Glycogen phase separation drives macromolecular rearrangement and asymmetric division in *Escherichia coli*

Yashna Thappeta[1,2,†], Silvia J. Cañas-Duarte[1,4,†], Haozhen Wang[1,4], Till Kallem[5], Alessio Fragasso[1,2], Yingjie Xiang[6], William Gray[6], Cheyenne Lee[6††], Georgeos Hardo[7,&], Lynette Cegelski[5], Christine Jacobs-Wagner[1,2,3,4*]

[†]These authors contributed equally to this work

[1]Sarafan Chemistry, Engineering, and Medicine for Human Health Institute, Stanford University, Stanford, CA, USA

[2]Department of Biology, Stanford University, Stanford, CA, USA

[3]Department of Microbiology and Immunology, Stanford University, Stanford, CA, USA

[4]Howard Hughes Medical Institute, Stanford University, Stanford, USA

[5]Department of Chemistry, Stanford University, Stanford, CA, USA

[6]Mechanical Engineering and Materials Science, Yale University, New Haven, CT, USA

[7] Department of Engineering, University of Cambridge, Cambridge, Cambridgeshire, UK

[*]For correspondence**:** jacobs-wagner@stanford.edu

Present address:

[††]Department of Molecular Genetics and Microbiology, Duke University, Durham, NC, USA

[&]Department of Biology, United Arab Emirates University, Al Ain, Abu Dhabi, UAE

ABSTRACT

Bacteria often experience nutrient limitation. While the exponential and stationary growth phases have been characterized in the model bacterium *Escherichia coli*, little is known about what transpires inside individual cells during the transition between these two phases. Through quantitative cell imaging, we found that the positions of nucleoids and cell division sites become increasingly asymmetric during transition phase. These asymmetries were coupled with asymmetric reorganization of protein, ribosome, and RNA probes in the cytoplasm. Results from live-cell imaging experiments, complemented with genetic and ^{13}C whole-cell nuclear magnetic resonance spectroscopy studies, show that preferential accumulation of the storage polymer glycogen at the old cell pole leads to the observed rearrangements and asymmetric divisions. Live-cell atomic force microscopy analysis, combined with in vitro biochemical experiments, suggests that these phenotypes are due to the propensity of glycogen to phase separate into soft condensates in the crowded cytoplasm. Glycogen-associated differences in cell sizes between strains and future daughter cells suggest that glycogen phase separation allows cells to store large glucose reserves without counting them as cytoplasmic space.

KEYWORDS

Asymmetric division/ bacteria/ glycogen/ nutrient limitation/ phase separation

INTRODUCTION

Spatial order is an inherent feature of living cells across the tree of life. In eukaryotic cells, this is exemplified by the presence of membrane-bound organelles. These cells also display extensive membrane-less organization, including that mediated by phase separation between various cellular components (Alberti & Hyman, 2021; Banani *et al*, 2017; Boeynaems *et al*, 2018; Hyman *et al*, 2014; Rostam *et al*, 2023). Although bacteria typically lack membrane-bound organelles in their cytoplasm, they exhibit spatial organization at multiple levels (Surovtsev & Jacobs-Wagner, 2018), in the form of protein localization, chromosome structure, and phase-separated condensates involving proteins and/or nucleic acids, to name a few (Azaldegui *et al*, 2021; Bakshi *et al*, 2012; Cohan & Pappu, 2020; Landgraf *et al*, 2012). While subcellular organization is particularly evident in bacteria that undergo developmental programs and/or have dimorphic life cycles (e.g., sporulating bacteria, asymmetrically dividing α-proteobacteria), even bacteria with comparatively simpler life cycles, such as *Escherichia coli* display spatial organization. For example, *E. coli* divides precisely in the middle of the cell through two separate mechanisms. The time-average pole-to-pole oscillation of Min proteins positions the FtsZ cytokinetic ring at mid-cell (Lutkenhaus, 2008; Shih & Zheng, 2013), while nucleoid occlusion prevents cell constriction over nucleoid regions (Woldringh *et al*, 1990). Furthermore, *E. coli* spatially organizes two of its most important cytoplasmic components: the chromosome and polysomes (mRNAs in complex with ribosomes engaged in translation). The chromosome, which compacts into a meshwork structure known as the nucleoid, is spatially positioned inside cells, either near the cell center prior to DNA replication or near the ¼ and ¾ cell positions after DNA replication and segregation

(Badrinarayanan *et al*, 2012; Bates & Kleckner, 2005; Sherratt, 2003). Polysomes adopt a near-opposite localization profile. They are depleted in the nucleoid and enriched in nucleoid-free regions (Azam *et al*, 2000; Bakshi *et al*, 2012; Chai *et al*, 2014). This anticorrelated pattern is thought to be mediated at least in part by the steric exclusion of polysomes from the nucleoid mesh (Mondal *et al*, 2011; Papagiannakis *et al*, 2025; Castellana *et al*, 2016). In contrast, smaller components such as free ribosomal subunits and cytoplasmic proteins can diffuse throughout the nucleoid unimpeded (Amselem *et al*, 2023; Bakshi *et al*, 2012; Sanamrad *et al*, 2014), resulting in homogeneous distribution throughout the cytoplasm. This archetypical macromolecular organization is reproduced every generation.

The bulk of our knowledge of *E. coli* (and other well-studied bacteria) has largely been derived from exponentially growing cultures. In their natural environments, *E. coli* and other bacteria often experience nutrient deprivation to which they must adapt (Dworkin & Harwood, 2022). In the laboratory, nutrient deprivation occurs in batch cultures when cells exit exponential growth and transition to stationary phase due to the limitation of an essential nutrient. Growth arrest, however, is not immediate. As nutrient availability decreases, cell growth slows progressively until the cell density reaches saturation, marking the onset of stationary phase (Dworkin & Harwood, 2022). During this transition, cells are thought to block new rounds of DNA replication before they stop dividing, ultimately entering stationary phase with a smaller size and lower chromosome content on average relative to their exponential phase counterparts (Åkerlund *et al*, 1995). Yet, the transition between exponential growth and stationary phase remains under-

characterized, especially at the single-cell and subcellular organizational levels. This study sets out to fill this gap in knowledge.

RESULTS

Population characteristics change along the culture growth curve.

We first used microscopy and DNA staining with 4',6-diamidino-2-phenylindole (DAPI) to quantify various cellular characteristics (cell area, nucleoid area, number of nucleoids per cell, fraction of dividing cells, intracellular positioning of the division site and of the nucleoid, etc.) along the growth curve of liquid cultures of *E. coli* at 30˚C in M9 medium containing 0.2% glucose, casamino acids and thiamine (M9gluCAAT). Under our experimental conditions, cultures exhibited exponential growth up to an optical density (OD) at 600 nm of about 1.0, after which population growth slowed down gradually until reaching saturating ODs around 3.0 (Fig 1A). While the culture might experience a diauxic shift in this medium when transitioning between exponential and stationary phases, we will hereafter refer to this period of sub-exponential growth (between ODs ~1 and ~3) as "transition phase" for simplicity (Fig 1A). This phase is more readily discernible in a logarithmic scale than a linear one (Fig 1A, inset), as it better highlights the deviation from exponential growth.

Imaging live cells from the same liquid culture at a high sampling resolution along the growth curve was technically impractical with our setup. Therefore, we imaged DAPI-stained cells (Fig 1B) from independent cultures at multiple ODs on different days and examined how various cellular characteristics may change as a function of the OD. As expected (Buchanan, 1918; Morita, 1990; Bakshi *et al*, 2021), we found that the average

cell area decreased with increasing OD (Fig 1C). The mean nucleoid area also decreased as cells entered transition phase (Fig 1D), as did the mean number of nucleoids per cell (Fig 1E). As a result, the fraction of cells with a single nucleoid increased in transition phase, reaching a plateau at OD ~ 1.5, before the cell density saturated (Fig 1F). Meanwhile, the fraction of cells undergoing constriction at the division site gradually decreased around the onset of transition phase (OD ~1) and continued to decrease until the culture reached stationary phase (Fig 1G). These results are consistent with cells undergoing one or more so-called ‘reductive divisions‘ after DNA replication initiation has stopped (Nyström, 2004; Nyström & Kjelleberg, 1989). This uncoupling between DNA replication and cell division explains the reduction in chromosome copy number per cell by the time the culture enters stationary phase (Åkerlund *et al*, 1995).

To our surprise, while the position of the cell constriction site was symmetric across cell populations sampled during exponential phase (OD < 1), it became increasingly asymmetric during sub-exponential growth in the transition phase (OD > 1) (Fig 1H). Transition phase cells with asymmetric constriction sites also displayed asymmetrically positioned nucleoids, creating larger DNA-free space at one pole than the other (Fig 1B, inset where the magenta arrowheads indicate the cell constriction sites). To quantify this asymmetric feature, we calculated the absolute distance between the nucleoid mid-point and the cell center, normalized by cell length. For cells with two nucleoids, we averaged their relative mid-points such that when the center of each nucleoid was positioned at the quarter cell positions, the mean mid-point was located at the cell center (see schematic in Fig 1I). In exponentially growing populations, the mean nucleoid mid-point was maintained close to cell center (Fig 1I, grey curves). In stationary phase, the nucleoid

position was more variable (Fig 1I, blue curves), as qualitatively noted before (Chai *et al*, 2014). The most striking phenotype was observed in transition phase when populations often displayed a bimodal distribution of nucleoid mid-points (Fig 1I, red curves). This result implies that the nucleoid mid-point tends to be closer to a pole than the cell center, confirming visual inspection (Fig 1B, inset).

Cells exhibit asymmetric intracellular distributions of ribosomes, RNAs, and cytosolic protein probes in transition phase.

Given the common offset in division site and nucleoid positioning in transition-phase cells, we wondered whether the intracellular organization of other macromolecules also changes when cells exit exponential phase. First, we examined the localization of mCherry-tagged ribosomal protein RplA and freely diffusing msfGFP in the cytoplasm. As expected, in exponential phase, msfGFP was distributed homogeneously throughout the cytoplasm while the RplA-mCherry signal was enriched outside the DAPI-stained nucleoid regions (Fig 2A). The latter is consistent with most ribosomes forming polysomes (Phillips *et al*, 1969; Mohapatra & Weisshaar, 2018) and polysomes being partially excluded from the nucleoid (Azam *et al*, 2000; Bakshi *et al*, 2012; Chai *et al*, 2014). In contrast, in transition phase, both msfGFP and RplA-mCherry signals were depleted from the cell pole farthest away from the asymmetrically localized nucleoid labeled with DAPI (Fig 2A). This depletion was confirmed quantitatively across the population ($n > 488$ cells) by calculating the normalized pole signal difference, which is the fluorescence signal at one (randomly selected) pole subtracted from the corresponding signal at the other pole, and divided by the average fluorescence in the cell. The distributions of normalized pole

signal differences were narrow and close to 0 in exponential phase for both msfGFP and RplA-mCherry (Fig 2B), consistent with near-equal concentrations of fluorescent markers between cell poles. In contrast, the distributions of the normalized pole differences were broader and bimodal in transition-phase cells (Fig 2B). In these cells, signal pole differences that were negative (positive) for msfGFP were also negative (positive) for RplA-mCherry (Fig 2B). This correlation (Spearman's correlation $\rho = 0.67$) indicates that the ribosomes and protein probes are preferentially depleted from the same pole in transition-phase cells. We observed the same intracellular reorganization in transition phase using other ribosomal protein fusions (RplA-msfGFP, RplA-mCherry, or RpsB-msfGFP) and another cytoplasmic protein probe (mScarlet-I) (Fig EV1A-B). Furthermore, GFP derivatives with surface net charges varying between -30 and +15, which reflect most of the range of net surface charges in the *E. coli* proteome (Schavemaker *et al*, 2017), were similarly enriched in the nucleoid region during transition phase (Fig EV1C). The comparable localization phenotype across cytoplasmic protein probes of different charges and genetic origins (Fig 2A, Fig EV1B-C) suggests that this subcellular reorganization is likely common among cytoplasmic proteins during transition phase.

To determine whether this change in localization pattern extends beyond ribosomes and cytoplasmic protein probes, we also assessed RNA localization in two ways. First, we used a cytosolic mutant variant of RNase E, RNase E ΔMTS, fused to mCherry (Strahl *et al*, 2015), based on the assumption that its localization would, at least in part, reflect that of its RNA substrates. RNase E, which is involved in the degradation of mRNAs and the processing of rRNAs (Strahl *et al*, 2015), is normally membrane-associated via a short membrane-targeting sequence (MTS) (Khemici *et al*, 2008).

Deletion of the MTS sequence releases the protein into the cytoplasm (Khemici *et al*, 2008). We found that in exponentially growing cells, a mCherry fusion to ΔMTS RNase E mutant exhibited various degrees of accumulation in nucleoid-free regions (Fig 2C). This localization pattern changed during transition phase, with RNase E ΔMTS-mCherry primarily colocalizing with the asymmetrically localized nucleoid, resulting in a marked depletion of the RNase E ΔMTS-mCherry marker at the pole most distal to the nucleoid (Fig 2C). This switch was confirmed at the population level by the drastic change in the distribution of the normalized pole signal differences between phases ($n \geq 3110$ cells, Fig 2D). The values in signal pole difference centered around 0 in exponential phase, indicating a near-equal distribution of probe signal between the cell poles. In contrast, the distribution became bimodal with peak values deviating from 0 (Fig 2D), indicative of pole depletion (Fig 2D), as observed for the ribosomes and protein markers (Fig 2B). Second, we imaged cells incubated with SYTO RNASelect, a membrane-permeable fluorogenic RNA dye that has been validated in *E. coli* (Bakshi *et al*, 2014). We found that the RNASelect signal, which was relatively homogeneously distributed in exponential-phase cells, exhibited depletion at a cell pole during transition phase (Fig EV1D).

So far, for our analyses of signal depletion at the cell poles, we used snapshot images where the pole identity was unknown and thus randomly assigned. To examine whether the pole selection is stochastic or deterministic, we carried out timelapse microscopy on transition-phase cells carrying RplA-GFP and a DNA-binding protein HupA fused to mCherry to visualize the nucleoid and ribosomes, respectively. These experiments revealed that the HupA-mCherry-labeled nucleoids of cells in transition phase remained closer to the new pole generated at division (Fig 2E, Video EV1). The

ribosome signal largely followed the nucleoid, resulting in ribosome depletion preferentially at the old pole (Fig 2E, Video EV1). This pattern was observed in 88.6% of all observed division events (695 out of 784), consistent with a deterministic pole selection.

The cytoplasmic reorganization in transition phase cannot be explained by membrane retraction or nucleoid association.

It was recently reported that, in stationary phase or upon acute starvation, the inner membrane of *E. coli* cells often retracts due to the sudden loss of cytoplasmic water and atrophy of the cytoplasmic volume (Shi *et al*, 2021). Therefore, we wondered whether a membrane collapse may explain both the observed nucleoid position asymmetry and the enrichment of cytoplasmic components in the nucleoid space in transition phase. Based on phase-contrast images and cell staining with MitoTracker Green, a fluorescent dye that labels the inner membrane (Shi *et al*, 2021), we found no evidence of membrane retraction driving fluorescent signal depletion at the poles during transition phase (Fig EV2A). In fact, membrane retraction was rare during this phase and observed in only 2 cells out of 3035.

Interestingly, when we generated filamentous polyploid cells in transition phase using the cell division inhibitor cephalexin (Hedge & Spratt, 1985; Pogliano *et al*, 1997; Rolinson, 1980), we observed that the ribosome (RplA-mCherry) and protein (msfGFP) probes colocalize with the nucleoids and are depleted in nucleoid-free spaces, including between nucleoids (Fig 2F). We confirmed this localization pattern for msfGFP using an FtsZ depletion strain as an orthogonal method to block cell division (Fig EV2B). Given the colocalization with the nucleoid, we questioned whether the observed rearrangement of

cytoplasmic components may be driven by direct or indirect association with the nucleoid. Two lines of evidence suggest otherwise. First, in filamentous polynucleoid cells, we occasionally observed a sharp accumulation of fluorescently labeled ribosomes and msfGFP in nucleoid-free space (Fig 2G, purple arrowhead and bracket area, respectively). Second, we noted that the intensity profiles of the msfGFP signal extend beyond that of the DAPI signal (Fig 2A). This was not due to the lower excitation wavelength of DAPI relative to that of the fluorescent protein probes, as the msfGFP signal also extended beyond the nucleoid signal labeled with HupA-mCherry (Fig 2H), which emits at a higher wavelength than msfGFP. Thus, the intracellular rearrangement of ribosomes and proteins in transition phase is not driven by an association with the nucleoid. Instead, it suggests that these cytoplasmic components are excluded by a cytosolic element that accumulates in nucleoid-free space during transition phase, particularly at the old pole when cells are allowed to divide.

Glycogen accumulation contributes to the transition-phase phenotypes.

In our search for the cytosolic element driving the observed intracellular reorganization in transition phase, we used whole-cell ^{13}C cross-polarization magic-angle spinning (CPMAS) solid-state NMR to compare the carbon composition of cells between exponential and transition phases. We found that in comparison to exponential-phase samples, transition-phase samples showed a large increase in carbon intensities in the ^{13}C CPMAS NMR spectra between 110 and 55 ppm (Fig 3A, top spectra), characteristic of polysaccharide contributions. We speculated that these carbon intensity increases might correspond to an accumulation of glycogen, a glucose polymer that *E. coli* cells can

accumulate under limitation of a nutrient such as nitrogen, sulfur, or phosphate (Preiss, 1984; Wilson *et al*, 2010; Preiss & Romeo, 1994; Zevenhuizen, 1966; Mulder *et al*, 1962; Sigal *et al*, 1964; Madsen, 1963). Furthermore, glycogen has been reported to accumulate at cell poles (Shively, 1974; Preiss, 1984; Liu *et al*, 2021b; Alonso-Casajús *et al*, 2006; Preiss & Romeo, 1994). Consistent with our speculation, the ^{13}C CPMAS NMR spectra of bovine and mussel-derived glycogen were consistent with the spectral changes observed in transition phase samples (Fig 3A, middle spectra). We then generated a glycogen-deficient strain (Δ*glgBXCAP*) by deleting the glycogen metabolic operon from the chromosome. The ^{13}C CPMAS NMR spectrum of transition-phase samples from this glycogen-deficient strain lacked the large carbon intensity increase observed in the wild-type (WT) strain (Fig 3A, bottom spectra), confirming that this peak corresponds to glycogen.

Next, we examined whether the accumulation of glycogen in transition phase drives the phenotypes we observed in that phase, starting with the asymmetries in cell constriction and nucleoid positioning. Since the extent of these asymmetries changes with the OD during transition phase (Fig 1H-I), we co-cultured WT and Δ*glgBXCAP* strains to compare their phenotypes at precisely the same OD. Cells from each strain carried a different fluorescent protein, either mVenus or mSCFP3, to allow their differentiation by fluorescence microscopy (Fig 3B). These strains also expressed HupA-mCherry for nucleoid visualization (Fig 3B). We found that the offset of cell constriction and nucleoid positions from the cell center was minimal for both glycogen-free (Δ*glgBXCAP*) and glycogen-producing (WT) cells in exponential phase (Fig. 3C-D, Mix 1). While the offsets considerably increased in transition phase for the WT cells, they did not for the mutant

cells (Fig 3C-D, Mix 1). We obtained similar results across biological replicates (Fig EV4, Fig EV5) or when the strain-identifying proteins mVenus and mSCFP3 were swapped between the WT and Δ*glgBXCAP* backgrounds (Fig 3C-D, Mix 2). The findings are consistent with glycogen production in transition phase driving the observed nucleoid and cell constriction asymmetries.

Deletion of the glycogen biosynthesis operon also abrogated the intracellular rearrangement of ribosomes (RplA-mCherry) and protein probes (msfGFP) in transition phase (Fig 3E to compare with WT data in Fig 2B). This was also true for the RNase E ΔMTS-mCherry marker (Fig 3F to compare with WT data in Fig 2D).

We reasoned that if the physical presence of glycogen at cell poles drives the transition-phase phenotypes, the severity of the phenotypes should correlate with the extent of glycogen accumulation across cells. To visualize glycogen in live cells, we built a glycogen biosensor and placed its synthesis under the control of the isopropyl β-D-1-thiogalactopyranoside (IPTG)-inducible promoter P_{tac} inserted on the chromosome. Inspired by a previous eukaryotic study (Skurat *et al*, 2017), we generated a translational mGFPmut3 fusion to the N-terminus of the starch/glycogen binding domain (CBM20) of the human protein Stbd1. We found that the basal expression from the P_{tac} promoter (i.e., without IPTG addition) was sufficient to visualize the glycogen sensor when cells reach transition phase, likely due to metabolic regulation (Bren *et al*, 2013; Grossman *et al*, 1998). In the absence of glycogen production, the distribution of the glycogen sensor remained diffuse throughout the cytoplasm of Δ*glgBXCAP* cells, similar to a free fluorescent protein such as mScarlet-I (Fig 3G). In contrast, glycogen accumulation in WT cells during transition phase resulted in the accumulation of the glycogen sensor in

nucleoid-free space, with its highest concentrations observed in regions from where mScarlet-I was depleted (Fig 3G). The anti-correlation of the fluorescent glycogen biosensor with both the nucleoid marker (DAPI) and the cytoplasmic protein probe (mScarlet-I) across cells (n = 3,591) was evident by their markedly negative values for the signal correlation factor (SCF) (Fig 3H), a metric that assesses the correlation between two signals at pixel resolution within individual cells (Gray *et al*, 2019). Furthermore, the glycogen sensor tended to accumulate more at one pole than the other and this asymmetric enrichment correlated strongly with the nucleoid offset from midcell (Fig 3I, n = 5794 cells, Spearman's correlation ρ = 0.75), consistent with glycogen accumulation effectively "pushing" the nucleoid closer to the opposite pole.

Another line of support for the physical presence of glycogen driving the transition-phase phenotypes was provided by observations of cephalexin-treated cells expressing the glycogen sensor and fluorescently labeled ribosomes. Whenever we observed a band of ribosome enrichment in nucleoid-free space (as first illustrated in Fig 2G), this region was flanked by glycogen accumulations (Fig 3J). This observation was independently corroborated using 2-NBDG (2-(N-(7-nitrobenz-2-oxa-1,3-diazol-4-yl)amino)-2-deoxyglucose) (Yoshioka *et al*, 1996b), a glucose analog that is taken up by *E. coli* (Yoshioka *et al*, 1996b, 1996a) where it can be incorporated into the glycogen polymer (Zhu *et al*, 2020). Upon uptake, the analog is modified to a non-fluorescent form, resulting in a loss of fluorescence signal (Yoshioka *et al*, 1996a) and leading to a low signal-to-noise ratio. Nevertheless, the signal intensity was sufficient to reveal 2-NBDG accumulations flanking ribosome enrichment in nucleoid-free space of cephalexin-treated cells producing glycogen during transition phase (Fig EV3).

316

317 **Preferential glycogen accumulation at the old cell pole through inheritance**
318 **contributes to cellular asymmetries.**

319 We hypothesize that the preferential accumulation of glycogen at the old pole through
320 inheritance over divisions (Boehm *et al*, 2016) causes the cellular asymmetries observed
321 during transition phase. To test this hypothesis, we performed microfluidic experiments
322 on a mother machine-like device in which we visualized the localization of both the
323 glycogen sensor and the nucleoids (HupA-mCherry) in single cells. For the analysis, we
324 focused only on the “mother” cells (i.e., those located at the closed end of the trenches,
325 see Fig 4A), as they can be tracked over many generations (Wang *et al*, 2010). By
326 connecting the microfluidic device to a liquid batch culture, the cells inside the trenches
327 experienced the same changes in nutrient levels during the exponential-to-stationary
328 phase transition as those in the batch culture (Fig 4A) (Bakshi *et al*, 2021). At the start of
329 imaging, exponentially growing mother cells already had a small, but detectable glycogen
330 sensor signal at the old pole (Fig 4B), presumably because these cells inherited the old
331 pole and its content at each division over many generations, resulting in a gradual build-
332 up. *E. coli* is indeed known to synthesize glycogen at a low (basal) rate under exponential
333 growing conditions (Wang *et al*, 2020) . Under our experimental conditions, mother cells
334 transitioned between exponential and stationary phases after 3 to 4 generations based
335 on cell growth measurements (Fig EV6). We found that mother cells increased the area
336 of glycogen sensor signal at the old pole at each generation (Fig 4C), consistent with a
337 progressive accumulation of glycogen due to inheritance at division combined with de
338 novo synthesis.

Furthermore, the nucleoid offset from midcell correlated with the area of glycogen sensor signal at the old pole, with both variables increasing over time (Fig 4D). This is in agreement with the preferential accumulation of glycogen at the old pole effectively "pushing" the nucleoid toward the new pole by mutual exclusion. As glycogen accumulation at the old pole increased at each generation (Fig 4C), so did the nucleoid position offset (Fig 4E). In contrast, the nucleoid position offset did not increase in the glycogen-devoid Δ*glgBXCAP* mother cells experiencing the same conditions in separate channels (Fig 4E). These observations are consistent with a causal relationship between glycogen accumulation and nucleoid position asymmetry. Consumption of glycogen during stationary phase (Fung *et al*, 2013; Wang *et al*, 2021, 2020) explains the gradual decline in nucleoid position asymmetry observed with prolonged time in this phase (Fig 1I, Fig EV5).

Nucleoid position asymmetry correlates with division asymmetry across cells

What promotes asymmetric division in cells in transition phase? We considered two possibilities. First, large accumulations of glycogen at the old pole may interfere with the pole-to-pole oscillatory behavior of MinD, which, through its binding partner MinC, is known to affect the position of the FtsZ cytokinetic ring on time average (Shih & Zheng, 2013; Lutkenhaus, 2008). Second, by effectively pushing the nucleoid toward the new pole, the accumulation of glycogen at the old pole may shift the division site toward the new pole through nucleoid occlusion, a fail-safe mechanism that prevents cell constriction over nucleoid regions, thereby avoiding chromosome scissoring events(Woldringh *et al*, 1990). We found the first possibility unlikely as MinD-GFP continued to oscillate from the

edge of one pole to the other in transition-phase cells even when nucleoid asymmetry was evident (Video EV2). The apparent lack of interference is presumably due to glycogen accumulations not adhering to the cytoplasmic membrane, allowing MinD-GFP to diffuse around them and interact with the membrane at the poles. To test the nucleoid occlusion hypothesis, we measured the positions of nucleoids (labeled with HupA-mCherry) and cell constriction sites relative to the cell center from snapshot images of transition-phase cells (where the pole identity is unknown and thus randomly assigned). We found these two variables to be highly correlated across the cell populations (Fig 5A), with a Spearman's correlation of $\rho > 0.58$ across replicates ($n = 6$ with $n > 278$ cells for each replicate), consistent with a mechanism in which the preferential enrichment of glycogen at the old pole promotes asymmetric division primarily by offsetting nucleoid positioning.

Glycogen accumulation leads to a corresponding cell size increase.

The preferential accumulation of glycogen at the old pole also affects the cytoplasmic organization of the cell by partially excluding ribosomes, proteins, and RNAs (Fig 3). If division were symmetric and produced two daughter cells of equal size, the daughter cell that inherits the glycogen-richer pole would therefore receive less cytoplasmic content than its sibling. However, analysis of constricting cells in transition phase revealed that the future daughter cells with more glycogen tended to be bigger than their future siblings with less glycogen (Fig 5B), with a Spearman's correlation $\rho = 0.54$ (P value = 0 n = 365 cells). While there was considerable noise in our measurements, a linear fit across the data suggested a near direct proportionality (i.e., slope ~ 1) between the difference in

glycogen amount and the difference in cell size between future daughter cells (Fig 5B). This cell size difference is unlikely to be due solely to a growth benefit associated with glycogen metabolism since it is generated in the mother cell before cell constriction is complete, i.e., when the cytoplasm (and thus, the metabolism) of the two future daughter cells is still shared (Fig 5B). Thus, cells do not appear to "count" glycogen accumulations as cytoplasmic space and effectively create extra (i.e., bonus) space to accommodate the large amount of glycogen produced in transition phase.

This bonus-space hypothesis predicts that glycogen-deficient cells should, on average, be smaller than WT cells producing glycogen. To test this prediction, we compared the size of glycogen-producing (WT) and glycogen-deficient (Δ*glgBXCAP*) cells grown in co-cultures (Fig 3B). Consistent with our hypothesis, co-cultures of mVenus-expressing WT and mSCFP3-expressing Δ*glgBXCAP* cells revealed that glycogen-deficient cells were smaller than glycogen-producing cells in transition phase (Fig 5C, Mix 1). We obtained similar results when the fluorophores were swapped between the WT and Δ*glgBXCAP* backgrounds (Fig 5C, Mix 2), indicating that the cell size difference was independent of the type of fluorescent protein used to identify cells. Smaller but statistically significant differences in cell area were also found between WT and Δ*glgBXCAP* cells in exponential phase (Fig 5C), which is consistent with basal glycogen accumulation during this growth phase (Wang *et al*, 2020).

We also found that the nucleoid signal occupies a considerably smaller fraction of the cytoplasm in glycogen-producing (WT) cells compared to the glycogen-deficient (Δ*glgBXCAP*) mutant, particularly in transition-phase cells. This notable difference is evident in single-cell images (Fig 3B, single-cell images) and is further demonstrated at

the population level by the lower nucleocytoplasmic (NC) ratios (defined by the nucleoid area divided by the cell area) in WT cells relative to Δ*glgBXCAP* cells (Fig 5D). This disparity was primarily attributable to the differences in cell size between the two strains during the transition phase (Fig 5C), as the nucleoid areas themselves were comparatively more similar (Fig. 5E).

Glycogen condensates exclude fluorescent proteins in vitro.

In the bacteriology literature, glycogen accumulations are often described as “granules” due to their round or oval shapes when visualized by electron microscopy (Preiss, 1984; Liu *et al*, 2021b; Alonso-Casajús *et al*, 2006; Preiss & Romeo, 1994). This term can give the impression of a solid. However, recent work in mammalian liver cells has reported that glycogen can undergo liquid-liquid phase separation in the cytosol (Liu *et al*, 2021a). Glycogen extracted from mouse livers has also been shown to undergo concentration-dependent phase separation in vitro when exposed to a crowding agent (Liu *et al*, 2021a). Given these results, we asked the following questions: Does glycogen form liquid condensates under in vitro conditions that mimic the *E. coli* cytoplasm? If so, can these glycogen condensates exclude proteins as they appear to do inside *E. coli* cells?

For our in vitro conditions, we focused on three aspects of the *E. coli* cytoplasm: glycogen concentration, ionic strength, and crowder concentration. Given that glycogen represents 0.75-1.2% of the cell’s wet weight in stationary phase after growth in lysogeny broth (Wang *et al*, 2019a; Neidhardt & Curtiss, 1996), we assumed the glycogen concentration range to be between 8 and 13 g/L based on a cell density of 1.1 g/mL (Baldwin *et al*, 1995) (see Table EV1). We elected to use glycogen from mussels because

of its commercial availability at a high (>99%) purity. We used a potassium phosphate buffer (pH = 7.0) that includes 85 mM NaCl, 250 mM KCl, 2.5 mM $MgCl_2$ and 0.1 mM $CaCl_2$ to reflect the ionic strength of the *E. coli* cytoplasm (Schultz *et al*, 1962; Alatossava *et al*, 1985; Gangola & Rosen, 1987; Szatmári *et al*, 2020). Hereafter, we refer to this solution as the "intracellular salt (IS) buffer". As a stand-in for cytoplasmic macromolecules, we used the synthetic biocompatible nonionic polymer polyethylene glycol (abbreviated to PEG or PEO depending on its molecular weight). PEG/PEO polymers are available in a broad range of molecular weights. Since size, rather than molecular weight, is the relevant variable for a crowding agent (Asakura & Oosawa, 1954, 1958; Sharp, 2015), we used dynamic light scattering to measure the hydrodynamic (Stokes) diameter of PEG and PEO polymers of different molecular weights in the IS buffer (Fig 6A). Our results agree well with an empirical relationship determined in deionized water (pH = 5.5) (Devanand & Selser, 1991) (Fig 6A, line), despite the differences in pH and ion concentrations of the solvents used.

We first chose 3 kDa PEG (~3 nm of diameter) to mimic proteins, which are the most abundant macromolecular crowders in the *E. coli* cytoplasm (Neidhardt & Curtiss, 1996) with diameters ranging between 2 and 6 nm (Erickson, 2009; Hink *et al*, 2000; Lukatsky & Shakhnovich, 2008). We found that glycogen (10 g/L), visualized by fluorescence microscopy using ConA-FITC labeling (Lvov *et al*, 1996; Becker *et al*, 1976), transitioned from a homogeneously mixed state in the solution to forming droplets as the concentration of 3 kDa PEG increased from 9 to 20 mM (Fig 6B). Consistent with the liver study (Liu *et al*, 2021a) , these droplets exhibited liquid-like behaviors, demonstrating fusion events on the minute time scale (Fig 6C, Video EV3). These fusion events resulted

in the coalescence of small condensates into larger ones at longer time scales (e.g., 30 min, Fig 6D), which is consistent with a liquid-liquid phase separation. Note that these images were captured near the glass surface to keep droplets in focus and facilitate their visualization. In this context, some fusion events resulted in the formation of oval-shaped droplets that did not immediately become spherical. This phenomenon is likely due to the interaction between the droplets and the glass surface, as the droplets within the liquid column remained spherical after fusion and only became less spherical after they settled on the glass surface (Video EV4). We also found that at higher 3 kDa PEG concentrations, glycogen underwent a second phase transition, in which the droplets collapsed into amorphous aggregates (Fig 6B). Timelapse imaging of these aggregates showed no evidence of fusion upon collision (e.g., Video EV5), consistent with a more solid-like form.

In addition, we confirmed that the phase separation of glycogen is dependent on its concentration. As shown in a phase diagram (Fig 6E), higher concentrations of glycogen required a lower concentration of crowder to form liquid droplets. By using PEG/PEO of higher molecular weights, we also demonstrated that the formation of glycogen droplets is sensitive to the size of the crowder (Fig 6F). For instance, at least 19 mM of 3 kDa PEG was required for liquid droplets to form, while the same could be achieved with only 150 μM of 100 kDa PEO or 10 μM of 1 MDa PEO. The two larger crowders (100 kDa and 1 MDa) were chosen based on their estimated diameters, which are ~30 nm and ~70 nm, respectively (Fig. 6A). These sizes closely resemble those of ribosomes in their free and polysome forms (Brandt *et al*, 2009; Nilsson *et al*, 1997).

As both proteins and ribosomes (mostly assembled into polysomes) are excluded from glycogen in vivo (Fig 3G-J), we hypothesized that the combined effect of their cellular

concentrations could lead to the phase separation of glycogen into droplets. Consistent with this hypothesis, combining the stand-in crowders (10 mM of 3 kDa PEG, 25 μM of 100 kDa PEO, and 5 μM of 1 MDa PEO) at biologically relevant concentrations for proteins, ribosomes, and polysomes (see Tables S1 and S2) induced the formation of glycogen droplets in vitro. In contrast, none of these crowders alone triggered droplet formation at the same concentrations (Fig 6G). Note that, for the 1 MDa PEO crowder, the concentrations required to drive droplet formation are above its "overlap" concentration (self-crowding) (see Materials and Methods) and thus our estimated diameter for this crowder (Fig 6A) is likely overestimated. Regardless of the crowder size used, glycogen condensation into droplets was found to be reversible: diluting the crowders after the droplets formed led to their rapid (< 1 min) disappearance (Fig 6H).

To test whether glycogen condensation into droplets could account for the exclusion of proteins observed in vivo, we added GFP to the solutions and analyzed the spatial distribution of fluorescence intensity relative to the phase-contrast signal of the glycogen droplets. We found that glycogen condensates at the glass surface partially excluded the fluorescent proteins (Fig 6I). This was also observed by performing z-stack imaging of the glycogen condensates suspended in the liquid column, in which protein exclusion remains observable despite the added background from the contribution of GFP molecules in surrounding focal planes (Video EV6). This protein exclusion was observed in all tested combinations of PEG/PEO crowder sizes (2.7–74 nm) and concentrations that led to glycogen condensate formation (Table EV3).

Glycogen condensates inside cells are as soft as the rest of the cytoplasm, unlike protein aggregates.

Our in vitro data, together with estimates of intracellular macromolecule concentration (Tables S1-2) and the shape of so-called glycogen "granules" in electron micrographs (Preiss, 1984; Alonso-Casajús *et al*, 2006), are more consistent with glycogen forming droplets (liquid-like condensates) over solid aggregates inside cells. Testing this hypothesis is, however, not trivial. The small size of bacterial cells makes it impractical to examine liquid-like behaviors such as droplet fusions in vivo, as is often done in eukaryotic cells (Alberti *et al*, 2018, 2019; Hoang *et al*, 2023; Liu *et al*, 2021a). Assays based on fluorescence recovery after photobleaching (FRAP) and single-molecule tracking have been implemented to probe the liquid-like properties of condensate-forming proteins inside live bacterial cells (Alberti *et al*, 2019; Wang *et al*, 2019b). However, while proteins can easily be covalently tagged to a fluorophore through genetic engineering, this is not the case for a polysaccharide such as glycogen. FRAP experiments using the glycogen sensor showed that the fluorescence of the labeled glycogen region recovered from photobleaching (Fig EV7A-B), with half-maximum recovery times of 11.6 ± 2.3 s (mean ± standard deviation, n = 70 cells, Fig EV7C). These values are consistent with FRAP analyses of liquid glycogen condensates in mammalian liver cells (Liu *et al*, 2021a). However, our FRAP measurements are inconclusive due to the non-covalent nature of the interaction between the fluorescent biosensor and glycogen. The observed FRAP dynamics may reflect not only the motion of labeled glycogen molecules but also the (unknown) binding/unbinding kinetics of the fluorescent biosensor to/from glycogen. The use of the fluorescent glucose analog 2-NBDG, which covalently incorporates into

glycogen (Fig EV3), is unfortunately not suitable for FRAP experiments. This analog is modified to a non-fluorescent form upon cell uptake (Yoshioka *et al*, 1996b, 1996a), leading to a low intracellular signal-to-noise ratio (Fig EV3).

Given these caveats, we turned to atomic force microscopy (AFM) to determine the material properties of glycogen condensates inside *E. coli* cells at the nanometric scale. Our first approach leveraged AFM-based subsurface imaging, which has been used to visualize nuclei and cytoskeletal structures in eukaryotic cells (Guerrero *et al*, 2019; Roduit *et al*, 2009). In this technique, the AFM tip indents the cell without puncturing the membranes, and the indentation is deep enough to detect subsurface structures or organelles through variations in their mechanical resistance to the deformation. We adapted this method to bacterial cells to generate two-dimensional (2D) depth-resolved stiffness maps of transition-phase cells (CJW7605) with glycogen condensates labeled with our green fluorescent glycogen sensor (Fig 7A). For comparison, we imaged two other strains, a glycogen-free (Δ*glgBXCAP*) strain (CJW7668) expressing the yellow fluorescent protein mVenus and a strain (CJW7798) overproducing a blue fluorescence protein, which results in the formation of protein aggregates. The location of these protein aggregates could be easily identified in fluorescence images by the region depleted in mTagBFP2 signal (white arrow, Fig 7B), as previously shown (Papagiannakis *et al*, 2025). All three strains were grown in co-culture to ensure that they experienced the same environment during transition phase, as cell density increases when cultures exit exponential growth (Shi *et al*, 2021). We used correlated fluorescence microscopy to distinguish between cell types (Fig 7B) and to identify the location of glycogen condensates and protein aggregates within cells (arrows, Fig 7B). For all analyzed cells,

545 the preservation of membrane integrity (i.e., no abrupt change in AFM cantilever
546 deformations) was confirmed by examining the force-distance curves (see examples in
547 Fig EV8), using a previously validated method (Janel *et al*, 2019). The 2D stiffness maps
548 revealed that protein aggregates are stiffer than the rest of the cytoplasm (black arrow,
549 Fig 7B). In contrast, the stiffness values were uniformly low across the 2D maps of cells
550 with glycogen condensates, similar to glycogen-free cells (Fig 7B).

551 In addition, we performed an analysis known as “stiffness tomography”, which
552 spatially maps changes in stiffness along the indentation depth (Roduit *et al*, 2009).
553 Comparative stiffness tomography revealed that intracellular regions with protein
554 aggregates became increasingly stiffer with indentation depth, unlike surrounding areas.
555 This indicates that protein aggregates are relatively stiff, consistent with a solid-like state.
556 In contrast, the same type of measurements for regions with glycogen condensates
557 showed a relatively uniform stiffness distribution along the indentation depth, comparable
558 to glycogen-free regions (Fig 7C).

559 Under these conditions, the average cell height across strains ranged from 600 to
560 700 nm (Fig EV9A), as determined by measuring the distance between the glass surface
561 and the AFM tip’s contact point with the cell surface. With subsurface imaging, our
562 measurements were limited to a depth down to 400 nm below the cell surface (Fig EV8A-
563 C). To examine the material properties of glycogen condensates and protein aggregates
564 in a more direct way, we used a sharper AFM tip to penetrate through the cell membranes
565 and directly interact with the intracellular content (Fig 7D). Such an AFM-based approach
566 has been used to measure the stiffness of nuclei inside eukaryotic cells (Liu *et al*, 2014;
567 Oak *et al*, 2025). Here again, we used correlated fluorescence microscopy to position the

AFM tip on and off the target sites (Fig 7D). First, we confirmed successful membrane penetrations indicated by an abrupt change in AFM cantilever deformations (see curve examples in Fig EV10), as prior studies have demonstrated (Penedo *et al*, 2021; Del Valle *et al*, 2020). For these cell puncturing experiments, we used a force of 10 nN as a setpoint, which resulted in an average penetration depth of about 500 nm (i.e., ~¾ of the cell depth) across intracellular regions with or without glycogen condensates (Fig EV9B). In areas containing protein aggregates, the penetration depth was reduced to ~400 nm due to the stiffness of these intracellular structures, which resist deformation more than the surrounding cytoplasm (Fig EV9B). To calculate the stiffness of each intracellular region, we determined the slope of the force-distance curves after the membrane puncture point and plotted the median stiffness values from multiple puncture events (n = 64) in the target regions ("On") or control regions ("Off") (Fig EV10, see also Materials and Methods). This analysis demonstrated that intracellular regions with protein aggregates ("On") are considerably stiffer than other areas of the cytoplasm ("Off") (Fig 7E). In contrast, regions with ("On") or without ("Off") glycogen condensates within the same cells exhibited similarly low stiffness values (Fig 7E). Collectively, our results suggest that the stiffness of glycogen condensates is considerably lower than that of protein aggregates and is comparable to that of other cytoplasmic regions, supporting a liquid-like rather than solid-like state.

DISCUSSION

Our quantitative analysis of transition phase at the subcellular and single-cell level reveals a picture of *E. coli* cell biology that departs from the textbook view in several ways.

The first difference relates to division. Asymmetric divisions are typically thought of as exceptions in the bacterial world, restricted to a small subset of bacteria that undergo developmental programs that produce either two functionally divergent daughter cells at each cell cycle (e.g., *Caulobacter crescentus*) or an endospore in response to starvation (e.g., *Bacillus subtilis*). In fact, *E. coli* is often used as the quintessential example of a symmetrically dividing bacterium. However, its division has primarily been examined during exponential growth. Our study shows that asymmetric division and production of daughter cells of unequal sizes become common in *E. coli* when the population exists exponential phase and enters transition phase under our experimental conditions (Fig 1H, Fig 3C, Fig 5A-B), likely contributing to the documented increase in cell size variability in stationary phase (Bakshi *et al*, 2021).

We propose that these asymmetric divisions occur because of the propensity of glycogen to spontaneously phase separate into condensates in crowded environments (Fig 6) (Liu *et al*, 2021a). In vitro, glycogen condensates can grow to very large sizes through fusion (Fig 6). Inside cells, their sizes are likely restricted by spatial constraints (cellular and nucleoid boundaries) and out-of-equilibrium thermodynamics (glycogen synthesis/degradation, cell growth/division). In principle, the accumulation of large glycogen condensates could occur in any DNA-free regions, as observed in polyploid filamentous (cell division-arrested) cells (Fig 3J). However, in untreated cells, cell division results in the inheritance of glycogen condensates, which, together with de novo synthesis, results in a gradual accumulation of glycogen at the old cell pole, effectively "pushing" the nucleoids closer to the new pole (Fig 4). In fact, such nucleoid pushing effect can be artificially exacerbated in exponential phase through mutation of the carbon

storage regulator gene *csrA*, which results in massive glycogen overproduction (Boehm *et al*, 2016). We propose that the nucleoid position offset generated by glycogen condensates promotes off-center division through nucleoid occlusion (Fig 5A). In stationary phase, this cellular asymmetry decreases and nucleoid positioning becomes more variable (Fig 1I, Fig EV5) due to glycogen consumption (Fung *et al*, 2013; Wang *et al*, 2021, 2020), allowing the nucleoid to diffuse more freely through the cytoplasm.

Cells in transition phase also diverge from the traditional picture with respect to their spatial organization of ribosomes/polysomes, proteins, and RNAs. In transition phase, these cytoplasmic components adopt a more asymmetric distribution (Fig 2, Fig EV1), which is largely caused by glycogen production (Fig 3-5). Our in vitro experiments suggest that glycogen does not have to assemble into a solid (i.e., a granule) to exclude protein probes, as liquid condensates achieve similar results in vitro (Fig 6I). In fact, based on our calculations (Tables S1-2) and in vitro experiments (Fig 6E-G), the physiological range of intracellular concentrations of proteins, ribosomes, and polysomes is compatible with the combined PEG/PEO concentrations needed for glycogen to phase separate into liquid condensates, but not to collapse into a solid state. Collapsing glycogen into aggregates requires crowder concentrations that well exceed the macromolecular concentration expected inside cells (Fig 6E, Tables S1-2). Furthermore, unlike the amorphous glycogen aggregates, the liquid condensates formed in vitro are morphologically consistent with the round and oval shapes of glycogen bodies observed in electron micrographs of starved cells (Alonso-Casajús *et al*, 2006). Consistent with our results, a preprinted study has shown that concentrating macromolecules in frog egg extracts by ≥ 1.4-fold demixes the cytoplasm into two liquid phases: a glycogen-enriched

637 phase and a ribosome-enriched phase (Pelletier *et al*, 2021). In *E. coli,* and presumably
638 other glycogen-producing bacteria, this cytoplasmic demixing may be even more likely,
639 as the bacterial cytoplasm is thought to be more crowded than the eukaryotic cytosol
640 based on fluorescent protein diffusion measurements (Elowitz *et al*, 1999; Swaminathan
641 *et al*, 1997; Potma *et al*, 2001; Konopka *et al*, 2009). Furthermore, our AFM
642 measurements suggest that the mechanical properties of glycogen accumulations within
643 cells align more closely with (liquid-like) cytoplasmic material than with solid aggregates.
644 Glycogen is well-known to provide a way for cells to store a large amount of
645 glucose without dramatically increasing the osmolarity of their cytoplasm, as a branched
646 glycogen polymer contains thousands of glucose residues (Bezborodkina *et al*, 2018).
647 Whether its phase separation into condensates is associated with beneficial or
648 detrimental implications for the cell is an interesting question that warrants further
649 exploration. For instance, since glycogen has viscogenic properties (Persson *et al*, 2020),
650 compartmentalization into condensates might prevent high levels of glycogen from
651 increasing the cytoplasmic viscosity, which could decrease macromolecular diffusion to
652 deleterious levels. Furthermore, if glycogen did not phase separate (i.e., remained soluble
653 and homogeneously distributed in the cytoplasm), the distribution of glucose reserves
654 between daughter cells would be equal. In contrast, our data suggest that phase
655 separation leads to an asymmetric distribution that increases with each division through
656 additive glycogen accumulation at the old pole (Fig 4). This unequal distribution endows
657 a fraction of the cell population with larger energy reserves, which may increase the
658 survival probability of the species under prolonged periods of duress. Glycogen has
659 indeed been reported to facilitate the adaptation of environmental, phototrophic, and

pathogenic bacteria to starvation and other stresses (Sekar *et al*, 2020; Bourassa & Camilli, 2009; Klotz *et al*, 2016; Klotz & Forchhammer, 2017; Gründel *et al*, 2012; Wang *et al*, 2020). As for the partitioning of other macromolecules, their exclusion from glycogen condensates does not appear to affect their distribution between daughter cells. This is because division becomes asymmetric in the presence of glycogen condensates; the larger the glycogen accumulation, the more asymmetric the division (Fig 5B), minimizing any potential detrimental disparity in cytoplasm partitioning between daughter cells. In effect, the cells appear not to “count” the space occupied by the glycogen condensates (Fig 5B).

The relevance of our work may extend beyond *E. coli*, as glycogen metabolism is widespread across bacteria (Almagro *et al*, 2015; Henrissat *et al*, 2002; Preiss & Romeo, 1990; Wang *et al*, 2019a; Wang & Wise, 2011). Induction of glycogen synthesis is a common response when a nutritional element such as nitrogen, sulfur, or phosphate becomes limiting (Holme *et al*, 1956, 1957; Strange *et al*, 1961; Mulder *et al*, 1962; Sigal *et al*, 1964; Madsen, 1963; Zevenhuizen, 1966). Given that bacteria often live in nutrient-fluctuating environments, our findings suggest that the cellular asymmetries in division and macromolecule distribution may be more prevalent in the bacterial world than currently appreciated. In addition, phase separation may be relevant to other bacterial storage polymers besides glycogen. Polyphosphate, an energy-rich anionic polymer, is a good candidate. It accumulates into intracellular bodies, often referred to as ‘granules’, in various bacteria (Albi & Serrano, 2016). Timelapse experiments on starved *Pseudomonas aeruginosa* cells have shown that these so-called granules decrease in number while increasing in size during de novo biogenesis, consistent with fusion events

683 and liquid behavior (Racki *et al*, 2017). Future exploration may shed light on the
684 prevalence, role, and implications of phase separation across storage polymers in
685 different bacteria.

686

687

688 **MATERIALS AND METHODS**

689 **Reagents and tools table**

Reagent/resource	Reference/source	Identifier or catalog number
Bacterial Strains		
F-lambda- ilvG- rfb-50 rph-1	(Jensen, 1993)	MG1655
MG1655 *rplA*::*rplA-gfp*	(Gray *et al*, 2019)	CJW4677
MG1655 *rne*::*rneΔMTS-mcherry*	This work	CJW5685
MG1655/pEB2-mScarlet-I	AddGene; deposited by Dr. Philippe Cluzel	104007
MG1655 *rplA*::*rplA-msfGFP*	(Gray *et al*, 2019)	CJW7020
MG1655 *rpsB*::*rpsB-msfGFP*	(Gray *et al*, 2019)	CJW7021
MG1655 *attB*::*PproC-msfGFP-FRT-kan-FRT*	This work	CJW7083
MG1655 *attB*::*PproC-msfGFP*	This work	CJW7275
MG1655 *rplA*::*rplA-mCherry*	(Gray *et al*, 2019)	CJW7324
MG1655 *rplA*::*rplA-mCherry attB*::*PproC-msfGFP*	This work	CJW7325
MG1655 *attB*::*PproC-msfGFP hupA*::*hupA-mCherry*	This work	CJW7326
MG1655 *rplA*::*rplA-mcherry*/pBAD-GFP(-30)	This work	CJW7485
MG1655 *rplA*::*rplA-mcherry*/pBAD-GFP(-7)	This work	CJW7486
MG1655 *rplA*::*rplA-mcherry*/pBAD-GFP(0)	This work	CJW7487
MG1655 *rplA*::*rplA-mcherry*/pBAD-GFP(+7)	This work	CJW7488

MG1655 *rplA*::*rplA-mcherry*/pBAD-GFP(+11a)	This work	CJW7489
MG1655 *rplA*::*rplA-mcherry*/pBAD-GFP(+11b)	This work	CJW7490
MG1655 *rplA*::*rplA-mcherry*/pBAD-GFP(+15)	This work	CJW7491
MG1655 *rplA*::*rplA-mcherry*/pBAD-GFP(+25)	This work	CJW7492
MG1655 Δ*glgBXCAP-FRT-kan-FRT*	This work	CJW7537
MG1655 Δ*glgBXCAP*	This work	CJW7587
MG1655 *lacY*(A177C) *araFGH*::*spec* Δ*lacI* Δ*araE araBAD*::*dCas9 galM* <PBBa-J23119-sgRNA(*ftsZ*)-(S. pyogenes terminator)-(*rrnB* terminator)> *gmpA attB*::*PproC-msfGFP*	This work	CJW7588
MG1655 Tn*7*::*Ptac-GFPmut3-CBM20 FRT-cat-FRT*	This work	CJW7601
MG1655 Δ*glgBXCAP* Tn*7*::*Ptac-GFPmut3-CBM20-FRT-cat-FRT*	This work	CJW7604
MG1655 Tn*7*::P_{tac}-*GFPmut3-CBM20* FRT-*cat*-FRT *hupA*::*hupA-mCherry FRT-kan-FRT*	This work	CJW7605
MG1655 Tn*7*:: *Ptac -GFPmut3-CBM20-FRT-cat-FRT*	This work	CJW7606
MG1655 Δ*glgBXCAP* Tn*7*::*Ptac-GFPmut3-CBM20 FRT-cat -FRT*	This work	CJW7607
MG1655 *hupA*::*hupA-mcherry*	This work	CJW7660
MG1655 Δ*glgBXCAP hupA*::*hupA-mCherry*	This work	CJW7661
MG1655 *hupA*::*hupA-mCherry* Tn*7*:: *PRpsL-mSCFP3-FRT-kan-FRT*	This work	CJW7665
MG1655 *hupA*::*hupA-mCherry* Tn*7*:: *PRpsL-mVenus-FRT-kan-FRT*	This work	CJW7666
MG1655 Δ*glgBXCAP hupA*::*hupA-mCherry* Tn*7*::*PRps-mSCFP3-FRT-kan-FRT*	This work	CJW7667
MG1655 Δ*glgBXCAP hupA*::*hupA-mCherry* Tn*7*:: *PRps-mVenus-FRT-kan-FRT*	This work	CJW7668
MG1655 Δ*glgBXCAP* /pEB2-mscarlet-I	This work	CJW7718

MG1655 *ΔminD minE::sfgfp-minD minE::frt kanR frt*	This work	CJW7872
MG1655 Δ*glgBXCAP rne*::*rneΔMTS-mCherry*	This work	CJW7877
MG1655 Δ*glgBXCAP rplA*::*rplA-mCherry attB*::P_{proC}-*msfGFP*	This work	CJW7878
MG1655 (DE3) *hupA*::*hupA-mcherry rplA*::*rplA-msfgfp-frt-kanR-frt*/ pET28:mTagBFP2-CmR	This work	CJW7798
MG1655 Tn*7*:: *PRpsL-mSCFP3-FRT-kan-FRT*	Gift from Johan Paulsson	JP1456
MG1655 Tn*7*::*PRpsL-mvenus-FRT-kan-FRT*	Gift from Johan Paulsson	JP1457
MG1655 *lacY*(A177C) *araFGH*::*spec* Δ*lacI* Δ*araE araBAD*::*dCas9 galM* <PBBa-J23119-sgRNA(*ftsZ*)-(S. pyogenes terminator)-(*rrnB* terminator)> *gmpA*	(Li *et al*, 2016)	SJ_XTL229
Recombinant DNA		
pBAD-GFP (-30)	(Schavemaker *et al*, 2017)	
pBAD-GFP (-7)	(Schavemaker *et al*, 2017)	
pBAD-GFP (0)	(Schavemaker *et al*, 2017)	
pBAD-GFP (+7)	(Schavemaker *et al*, 2017)	
pBAD-GFP (+11a)	(Schavemaker *et al*, 2017)	
pBAD-GFP (+11b)	(Schavemaker *et al*, 2017)	
pBAD-GFP (+15)	(Schavemaker *et al*, 2017)	
pBAD-GFP (+25)	(Schavemaker *et al*, 2017)	
pEB2-mScarlet-I	AddGene	104007
pkD13-msfGFP	(Gray *et al*, 2019)	
pET28:mTagBFP2-CmR	(Papagiannakis *et al*, 2025)	
Oligonucleotides		
pNDL-1-Ptac-GFPmut3-CBM20 FRT-CmR-FRT	Integrated DNA Technologies	See Table EV5
Primers for strain construction	Integrated DNA Technologies	See Table EV6

Chemical, Enzymes and other reagents		
P1 phage	ATCC	25404-B1
Ampicillin	Fisher Scientific	BP1760-25
Kanamycin	Sigma-Aldrich	K1377-25G
Chloramphenicol	Sigma-Aldrich	C0378-25G
4′,6-diamidino-2-phenylindole (DAPI)	ThermoFisher	D1306
2-NBDG	Cayman Chemical Company	11046
MitoTracker Green	ThermoFisher	M7514
SYTO RNASelect	ThermoFisher	S32703
Cephalexin	Sigma-Aldrich	C4895
PEG1500	Sigma-Aldrich	81210-500G
PEG3000	Sigma-Aldrich	8190151000
PEG4000	Hampton Research	HR2-605
PEG6000	Sigma-Aldrich	81253-250G
PEG8000	Sigma-Aldrich	89510-250G-F
PEG10000	Sigma-Aldrich	81280-1KG
PEG20000	ThermoFisher	A17925.0B
PEG35000	Sigma-Aldrich	81310-1KG
PEO100000	Sigma-Aldrich	181986-250G
PEG1000000	Sigma-Aldrich	372781-250G
Glycogen	Millipore Sigma	361507-1ML
FITC-ConA	(Sigma-Aldrich	C7642-2MG
Pluronic® F-108	Sigma-Aldrich	542342-250G
GFP	ThermoFisher	A42613
mCherry	Abcam	AB199750
Software		
Oufti	(Paintdakhi *et al*, 2016)	https://oufti.org/
MATLAB R2024b	MathWorks	https://www.mathworks.com/products/matlab.html
ImageJ	National Institute of Health	https://fiji.sc/
Python 3	Phyton Software Foundation	https://www.python.org/
SyMBac	(Hardo et al, 2022)	https://symbac.readthedocs.io/en/latest/intro.html

Other		
Custom-made functions and scripts	This study	https://github.com/JacobsWagnerLab/published/tree/master/Thappeta_Canas-Duarte_et_al_2025

690
691
692
693

694 **Methods and protocols**

695 ***Bacterial strains and growth conditions***

696 Bacterial strains and descriptions of their constructions can be found in Tables S4 and 5.
697 P1 transductions were performed as previously described (Thomason *et al*, 2007) with
698 the exception that donor strains were grown without glucose supplementation. A lysate
699 of P1 phages was obtained from ATCC (25404-B1). Oligomers used for polymerase chain
700 reactions (PCR) are listed in Table EV6. Lambda red recombination was performed as
701 previously described using the pKD46 (Datsenko & Wanner, 2000) or pSIM6 plasmids
702 (Diner *et al*, 2011). Unless otherwise indicated, cells were grown at 30°C in M9 medium
703 (26.11 mM Na_2HPO_4, 22 mM KH_2PO_4, 8.55 mM NaCl, 18.7 mM NH_4Cl, 2 mM $MgSO_4$ and
704 0.1 mM $CaCl_2$) supplemented with 0.2% glucose, 0.1% casamino acids, and 1 µg/ml
705 thiamine (M9gluCAAT). Cells were first inoculated in the appropriate growth medium and
706 grown to stationary phase in culture tubes. They were then re-inoculated into fresh media
707 by diluting at least 10,000-fold and grown until they reached the indicated optical density
708 (OD) at 600 nm. When appropriate, ampicillin (100 µg/mL), kanamycin (50 µg/mL), or
709 chloramphenicol (30 µg/mL) was added to the media for selection.

Strains expressing green fluorescent proteins with different net charges (Schavemaker *et al*, 2017) were grown in M9gluCAAT, and fluorescent protein expression was induced with 0.4% arabinose upon re-inoculation of stationary phase cultures. Given the richer medium condition from the addition of arabinose, the transition phase OD ranged from 2.9 to 3.5 instead of 1.2 to 2.7.

FtsZ depletion experiments were conducted using strain CJW7588 in the presence of 0.2% arabinose. For exponentially growing cultures, arabinose was added for the equivalent of 2-3 doublings. For transition-phase cultures, arabinose was added in late exponential phase (~OD 0.4-0.5) and imaged ~5 h later when cultures reached transition phase ODs (the equivalent of 2-3 doublings) on an agarose pad made of spent medium.

Dyes and labels

To label the nucleoid, cells were incubated with 1 µg/ml 4′,6-diamidino-2-phenylindole (DAPI) for 10 min prior to imaging. To visualize intracellular 2-NBDG localization, cells were grown in M9CAAT supplemented with 0.2% L-arabinose to the desired OD and incubated with 10 µM 2-NBDG for 10 min, then washed twice in prewarmed spent medium filtered with a 0.22 µm filter. For the following dyes, concentrations were increased when used on transition-phase cells as cell permeability seemed to decrease with increasing ODs, consistent with a previous report (Bakshi *et al*, 2014). To visualize the inner membrane of *E. coli* cells, MitoTracker Green (Shi *et al*, 2021) was added to the cell culture at a final concentration of 100 nM (exponential phase) or 1 µM (transition phase) and incubated for 30 min prior to imaging. To label RNA, SYTO RNASelect was used at

a final concentration of 500 nM (exponential phase) or 2.5 µM (transition phase) for 10 min and washed twice in filtered spent medium (Bakshi *et al*, 2014) prior to imaging.

Cephalexin treatment

For cephalexin treatment of exponentially growing cultures, the antibiotic (50 µg/mL) was added for the equivalent of 2-3 doublings. For transition phase samples in M9gluCAAT, cells were incubated with cephalexin (50 µg/mL) in late exponential phase (~OD 0.4-0.5) and imaged ~5 h later when cultures reached transition phase (the equivalent of 2-3 doublings) on agarose pads made of spent medium containing cephalexin.

Co-cultures

For co-cultures experiments related to Fig 3B-D, Fig 5 A, C, D, and E, and Fig EV4 and EV5, cells of four strains (CJW7665-7668), each expressing a different fluorescent protein in either the WT or Δ*glgBXCAP* background, were inoculated in 2 mL of M9gluCAAT and grown overnight at 30°C with shaking (220 rpm). Each culture was then diluted 1:10,000 into fresh 2 mL cultures and returned to the shaker until they reached an OD of ~0.1. Samples of WT and glycogen-devoid strains were mixed proportionally to their ODs to create a ~50:50 mixture. For these experiments, two types of mixtures were used: one included WT cells expressing mSCFP3 and mutant cells expressing mVenus, while the other included WT cells expressing mVenus and mutant cells expressing mSCFP3. Mixtures were made independently in three biological replicates. Each mixture was then diluted 1:10,000 into 50 mL of medium in a 250 mL flask and returned to the shaker.

754 Samples were taken at OD of ~2.6 for transition phase. Samples were prepared for
755 imaging on agarose pads as described above.

756 For the AFM experiments related to Fig 7, WT cells expressing the glycogen
757 sensor (CJW7605), *ΔglgBXCAP* cells expressing the glycogen sensor (CJW7604) or
758 mVenus (CJW7668), and cells overexpressing mTagBFP2 (CJW7798) were inoculated
759 separately in 2 mL of M9gluCAAT medium and grown overnight at 30°C with shaking
760 (220 rpm). Mixtures of the three cell types were made and diluted 1:100,000 into 50 mL
761 of medium in a 250-mL flask and returned to the shaker. When the mixtures reached an
762 OD of ~0.5, IPTG was added to a final concentration of 100 mM to induce the
763 overexpression of mTagBFP2. Cultures were returned to the shaker and allowed to reach
764 a final OD of ~1.6. Samples were imaged in agarose pads containing filtered spent
765 medium (OD600 ~ 1.7) to verify the presence of protein aggregates in cells with
766 mTagBFP2 fluorescence.

767

768 ***Microscopy***

769 Unless otherwise indicated, cells were imaged on 1.5% agarose pads made with the
770 appropriate spent growth medium. For samples with high cell density in late transition or
771 stationary phase, cells were diluted in warm filtered spent medium prior to spotting on an
772 agarose pad for ease of cell segmentation.

773 Microscopy was performed using Nikon inverted microscope set-ups controlled by
774 the NIS-Elements AR software, with the following specifications. One of the set-ups
775 consisted of a Nikon Ti2-E inverted microscope equipped with a Perfect Focus System
776 (PFS), a motorized stage, a 100x Plan Apo 1.45NA Ph3 oil objective, a Photometrics

Prime BSI back-illuminated sCMOS camera, a Lumencor Spectra III LED light engine excitation source, a polychroic mirror (FF-409/493/596-Di02 for by Shemrock) combined with a triple-pass emitter (FF-1-432/523/702-25 by Shemrock) for GFP/DAPI/mCherry, and a polychroic mirror (FF-459/526/596-Di01 by Shemrock) combined with a triple-pass emitter (FF01-475/543/702-25 by Shemrock) for CFP/YFP/mCherry. The temperature was set and maintained at the indicated value using a temperature chamber (Okolabs). The second microscope set-up consisted of a Nikon Eclipse Ti microscope equipped with a Hamamatsu ORCA-Flash 4.0 camera, a 100X objective (Nikon, OFN Ph3 DM, N.A. 1.45) and a Spectra X light engine (Lumencor). The following Chroma filter sets were used to acquire fluorescence images: DAPI (excitation ET350/50x, dichroic T400lp, emission ET460/50 m), GFP (excitation ET470/40x, dichroic T425lpxr, emission ET525/50 m) and mCherry/TexasRed (excitation ET560/40x, dichroic T585lpxr, emission ET630/75 m). The temperature was maintained at 30°C using a customized enclosure and temperature controller (Air-Therm SWT, World Precision Instrument) for timelapse imaging. The temperature was also maintained for snapshots, but it did not affect transition-phase phenotypes in the time window required for imaging (under 12 min).

Image processing and analysis

For sample images with cell contours on agarose pads, cells were detected from phase contrast images using the open-source software package Oufti (Paintdakhi *et al*, 2016). For the images shown in the figures, fluorescent image background subtraction was done using Fiji (Schindelin *et al*, 2012) and a sliding paraboloid with a rolling ball radius of 50

pixels. Cell signal intensity profiles were generated using Oufti's signal output divided by the total signal intensity to calculate relative signal, which was plotted for individual cells.

For all experiments on agarose pads, cells were segmented from phase contrast images using the SuperSegger-Omnipose software (https://github.com/tlo-bot/supersegger-omnipose)(Stylianidou *et al*, 2016; Cutler *et al*, 2022). The software's pre-trained *bact_phase_omni* model (Cutler *et al*, 2022; Stylianidou *et al*, 2016) was retrained in-house prior to usage due to its tendency to split cells prematurely before cell division was completed, as determined based on visual inspection. Model retraining was carried out in two steps. First, images of CJW7606 cells (OD = 2.83) grown in M9gluCAAT at 30°C were collected on agarose pads containing M9gluCAAT. Cells from 11 fields of view (each of 2048x2048 pixels, ~100-250 cells per field of view) were segmented using the pre-trained model *bact_phase_omni*. The obtained masks were visually inspected, and when the pre-trained model was splitting cells too early, the cell masks were merged back into one single mask using a custom MATLAB code (LabelsMerge_ConstrictingCells.m). The corrected 2044x2048-pixel images (both phase contrast images and cell masks) were then divided into smaller 510x512-pixel images. The dataset was further augmented by performing image rotations (90°, 180°, and 270°), resulting in 704 images. This initial training dataset was then used to retrain Omnipose from scratch (with parameters: n_epochs = 4000; tyx = 224,224; batch_size = 16; learning_rate = 0.1, see details in https://omnipose.readthedocs.io) to generate a preliminary model. In the second step, the retrained model was used to re-segment the publicly available *bact_phase* training dataset (https://osf.io/xmury/) that was originally

used to train *bact_phase_omni*, including additional images of cells with extreme phenotypes (e.g., with bright intracellular regions in phase contrast images).

This generated a larger dataset with a broad spectrum of cell morphologies. The obtained segmented images were then manually curated to eliminate poorly segmented cells. Finally, both training datasets (the first one created in-house and the one re-segmented from *bact_phase*) were used to retrain Omnipose from scratch (n = 1249 images, with parameters: n_epochs = 4000; tyx = 224,224 ; batch_size = 16; learning_rate = 0.1). The resultant model (*merge_model_omni*) and the Python code used for curating (screening_good_bad.py) and generating the training datasets (generate_training_dataset.py) are available on GitHub (https://github.com/JacobsWagnerLab/published/tree/master/Thappeta_Canas-Duarte_et_al_2025).

Unless specified otherwise, *merge_model_omni* was used to segment cells across experiments. After segmentation, the resulting cell.mat files and the generated labels (masks.png) were imported to MATLAB, organized into structures, and further analyzed using custom scripts. Morphological features including cell length, cell area, cell width, and circularity were extracted from the cell labels using MATLAB's function *regionprops()* and used to filter out incorrect segmentations. For each experiment, histograms were generated for each of the above-mentioned features, and the appropriate thresholds used for filtering were modified accordingly.

The mid-cell axis of each cell was calculated using a bivariate fit to the distance matrix of the cell mask and used to identify the location of the cell centroid. For all cells, the distance between the mid-cell axis and the mask outline of each vertical half of the

844 cell was computed, smoothed, inverted, and used to identify peaks (function findpeaks(),
845 with parameters MinPeakProminence = 0.1 and MinPeakDistance = 15). For constricting
846 cells, the division plane (constriction site) was then localized using the location of
847 identified peaks on each cell half. Constriction offset was then determined by measuring
848 the absolute distance between the construction site and the cell centroid, followed by a
849 normalization by the cell length.

850 Nucleoids were initially segmented using Otsu, after which nucleoid objects were
851 refined by calculating the distance transform (function bwdist()) of the preliminary nucleoid
852 mask and applying the watershed transformation (function watershed(), using
853 connectivity = 4) on the inverse of the calculated distance transform. Binary opening,
854 closing, and fill operations were applied on the nucleoid mask. For cells with multiple
855 nucleoids, the nucleoid centroid was defined as the mid-point between the pair of the
856 most distal nucleoid objects. Nucleoid asymmetry was then determined by measuring the
857 absolute distance of the nucleoid mid-point to the cell's centroid, which was then
858 normalized by the cell length. The analysis described above was performed using the
859 custom MATLAB script PostSGO_AgarPad_FigureOne_AllODs.m.

860 To quantify the signal distribution of the different reporters used in this study, we
861 estimated both the signal correlation function (SCF) (Gray *et al*, 2019) and the normalized
862 signal difference between the two cell poles. To calculate the SCF, the centerline was
863 used to define a rectangular mask with a width of 4 pixels and a length equal to the cell
864 length minus 5 pixels from each cell pole. The SCF mask was then used to extract the
865 signal intensity from the fluorescence images. The correlation coefficient was then
866 calculated between the corresponding signals using the function corrcoef(). Likewise, the

867 normalized pole difference was calculated by defining two masks, each encompassing
868 the region between the cell pole and the cell centroid that corresponds to 30% of the cell
869 length. To avoid boundary effects, the pole masks were eroded by 2 pixels. As described
870 above, the masks were used to extract the signal intensity of the corresponding
871 fluorescence images. The normalized pole signal difference was then calculated by
872 subtracting the average intensity between the poles and dividing it by the average signal
873 intensity for the whole cell. These analyses were performed using a custom MATLAB
874 script PostSGO_PoleRatio_SCF_AllCells_20250615.m. The Spearman correlation
875 coefficient between the normalized signal intensities of free msfGFP and RplA-mCherry
876 was calculated using the corr() function, and the contour plot was obtained using a
877 MATLAB script (ContourPlot_20250311.m).

878 Time-lapse agarose pad data were analyzed as described above, with added
879 lineage/cell polarity tracking. Tracking was performed by first identifying lineages
880 (microcolonies) through spatial clustering using the MATLAB DBSCAN (Density-Based
881 Spatial Clustering of Applications with Noise) algorithm (epsilon = 45 and minpts = 4) and
882 then using the built-in genealogy information calculated by Supersegger within each
883 lineage. To track the polarity (old vs new pole) of the cells, cells were oriented vertically,
884 and the top-most pole was assigned as pole 1 and the bottom-most pole as pole 2. Cells
885 present at the beginning of the time-lapse sequence were labeled as generation zero,
886 and each of their daughters was labeled as generation one, and so forth. A total of three
887 divisions were analyzed, and polarity was assigned accordingly. Normalized pole signal
888 differences were calculated as described previously. This analysis was performed using
889 the custom MATLAB script PostSGO_AgarPAD_TL_20250613.

The degrees of both constriction position and nucleoid mid-point asymmetry in the WT strain were analyzed for each co-culture (Mix 1 and Mix 2) in transition phase using a MATLAB code (PostSGO_MixesConstriction_20240312.m). For this analysis, constricting cells were identified as described above using the centerline to determine the constriction position and the cell centroid. The HupA-mCherry signal in each constricting cell was used to segment the nucleoid and calculate its centroid. The offsets between the constriction position and the cell centroid, and between the nucleoid mid-point and the cell center were calculated and normalized by the length of each constricting cell. The Spearman correlation coefficient and the isocontours were then calculated between the relevant variables as described above.

For the microfluidic experiments, cell segmentation was performed using Omnipose. For this purpose, we retrained Omnipose using a two-step approach. First, a set of synthetic micrographs of bacteria in a mother machine-like system was generated using SyMBac (Hardo *et al*, 2022). The image simulation parameters were set to match that of the optical system previously described. Individual mother machine images were then tiled, along with their corresponding ground truth masks to produce a training dataset of simulated micrographs (n = 150). These synthetic micrographs were then used to retrain Omnipose from scratch. This first model was then used to segment real (non-synthetic) phase-contrast images of cells in our mother machine microfluidics system. The obtained segmentation results were then manually curated (screening_good_bad_trenches.py), augmented by mirroring individual trenches along their y-axis to double the size of the training data, and tiled back together in images containing five trenches (create_training_dataset_trenches.py), to produce an image

dataset of 237 images. Both empty and cell-filled trenches were included in this final dataset. Finally, Omnipose was retrained from scratch using both the original synthetic images, as well as the curated and augmented real images, to generate the final Omnipose model (MM_model_omni; n = 423 images, with parameters: tyx = 224,224; batch_size = 16; learning_rate = 0.1).

To improve the accuracy of segmentation, fields of view were cropped and aligned using the pre-segmentation modules of Supersegger. After segmentation, the mother-cell lineages were extracted and analyzed using a custom MATLAB script (PostSGOMM_GC.m). Briefly, lineages were initially identified using the MATLAB DBSCAN function (epsilon = 25 and minpts = 10). From there, mother cells were identified in each lineage and tracked throughout all acquired time points. Only lineages with successfully segmented mother cells and tracking across all (84) frames (84) were considered for the analysis. Instantaneous growth rates were calculated using a linear fit to the log-transformed cell lengths. The normalized nucleoid offset and glycogen area were calculated as described above.

The correlation between polar glycogen accumulations and the nucleoid offset was analyzed from snapshot images of CJW7606 cells (OD 2.83) that were segmented using a combination of SuperSegger-Omnipose and a MATLAB script (PostSGO_GlycogenSensorAllCells_20240312.m), in which the centerline of each cell was calculated as described above. Fluorescent signals from the glycogen sensor and HupA-mCherry were used to segment the areas of glycogen accumulations and the nucleoids, respectively. The difference between the glycogen sensor area for each cell pole was then calculated. Nucleoid offset was determined from the distance between the

nucleoid mid-point and the cell center. The Spearman correlation coefficient between the two variables was calculated and the contour plot was plotted using a MATLAB script (ContourPlot_20240312.m).

To examine the correlation between polar glycogen accumulations and asymmetric division, constricting cells in transition phase were identified, curated, and analyzed using a custom MATLAB code (PostSGO_GlycogenSensorConstriction_20240312.m). In short, the centerline of each cell was calculated as described above and was used to identify the location of the cell constriction plane. Fluorescence signal was extracted from each cell area flanking the division side (i.e., the future daughter cells) and used to create a mask for the glycogen sensor signal. The differences between each future daughter cell's area and between the glycogen sensor signal areas at each pole were used to calculate the Spearman correlation coefficient. Principal components regression was used to calculate the linear regression shown in Fig 6B.

Whole-cell NMR sample preparation and solid-state NMR measurements

Overnight cultures of each bacterial strain were prepared and diluted at least 10,000-fold into 300 mL of the appropriate fresh medium in a 1-L flask. To achieve similar final quantities of biomass, two flasks were prepared identically for exponential-phase cultures and one flask was prepared for the higher cell density transition-phase samples. Cells were pelleted by centrifugation at 10,000 *g* at 4°C for 10 min and washed twice in cold phosphate-buffered saline (PBS). Each final sample cell pellet was collected in a 50 mL

tube, stored at -80°C, and subsequently lyophilized and packed into a magic-angle spinning NMR rotor.

Solid-state ^{13}C CPMAS NMR (Schaefer & Stejskal, 1976) experiments were performed using an 89-mm bore 11.7 T magnet (Agilent Technologies) with an Agilent triple resonance BioMAS probe and DD2 console (Agilent Technologies). Samples were spun at 7143 ± 3 Hz at room temperature in thin-walled (36 µL capacity) 3.2-mm outer diameter zirconia rotors. Cross polarization (CP) was performed with a ^{13}C field strength of 50 kHz and a ^{1}H field strength centered at 57 kz with a 10% ramp for the contact time of 1.5 ms. ^{1}H decoupling was performed with two-pulse phase-modulated (TPPM) (Bennett *et al*, 1995) decoupling at 83 kHz. All CPMAS experiments were obtained using a recycle delay of 2 s. Free induction decays were processed using 80 Hz exponential line broadening prior to Fourier transformation. Spectrometer chemical shift referencing was performed by setting the high-frequency adamantane peak to 38.5 ppm (Morcombe & Zilm, 2003).

Intracellular salts buffer

To mimic the ionic strength of the *E. coli* cytoplasm, a potassium phosphate buffer (PPB) was prepared and supplemented with the appropriate concentrations of intracellular salts. For this, 200 mL of 1 M stock PPB (pH = 7.5) was prepared by mixing 25.63 g of K_2HPO_4 and 7.2 g of KH_2PO_4 in MilliQ water. For the intracellular salts buffer (referred to also as IS buffer), a 5X stock was prepared by mixing the 1 M PPB stock to a final 200 mM concentration with 0.425 M NaCl, 1.25 M KCl, 12.5 mM $MgCl_2$ and 0.5 mM $CaCl_2$ (Alatossava *et al*, 1985; Gangola & Rosen, 1987; Schultz *et al*, 1962; Szatmári *et al*, 2020).

Dynamic light scattering measurements

The hydrodynamic diameter of purified mussel glycogen (Sigma-Aldrich 361507-1ML) and commercially available PEG/PEO particles with varying molecular weights was measured using a NanoBrook Omni device. Stock solutions of PEG1500 (Sigma-Aldrich 81210-500G), PEG3000 (Sigma-Aldrich 8190151000), PEG4000 (Hampton Research HR2-605), PEG6000 (Sigma-Aldrich 81253-250G), PEG8000 (Sigma-Aldrich 89510-250G-F), PEG10000 (Sigma-Aldrich 81280-1KG), PEG20000 (ThermoFisher A17925.0B), and PEG35000 (Sigma-Adrich 81310-1KG) (30% w/v) were prepared in MilliQ water. Stock solutions 5% and 2.5% w/v were made of PEO100000 (Sigma-Aldrich 181986-250G) (5% w/v) and PEG1000000 (Sigma-Aldrich 372781-250G) (2.5% w/v. When needed, solutions were incubated at 42°C for 1 h to help homogenization.

For measurements, samples were diluted to a final volume of 10 mL to generate a final concentration of 6% (1.5 kDa PEG and 3 kDa PEG), 3% (4 kDa PEG),1.5% (6 kDa PEG, 8 kDa PEG, 10 kDa PEG, 20 kDa PEG and 35 kDa PEG), 0.25% (PEO 100 kDA) or 0.025% PEO 1MDa in either MilliQ water (pH = 6.5) or in the 1X IS buffer (pH = 7.0). Dilutions of the samples were made to ensure that measurements with each PEG/PEO crowder were done with concentrations below their overlap concentrations to avoid self-crowding artifacts in our measurements (de Gennes & Witten, 1980; Julius *et al*, 2019; Smith *et al*, 2023). The hydrodynamic diameter of glycogen was measured in the same IS buffer at a concentration of 2 g/L. To remove dust or other particles that could affect the measurements, all samples were double-filtered, first with a 0.22 µm filter followed by a 0.1 µm filter. Each sample (1 mL) was loaded into a cuvette and sealed with a lid.

Samples were measured in triplicate for 300 ms at 25°C using a 90-degree angle for the detector.

Preparation of the microfluidic chips

The microfluidic device used in this study was cast from an epoxy mold kindly shared by the Paulsson lab (Bakshi *et al*, 2021). In this device, the feeding channel has a width of 350 μm and a height of 25 μm. Cell trenches have a width of 1.3 μm, a length of 25 μm, and a height of 1.25 μm. Polydimethylsiloxane (PDMS), a silicone elastomer composed of dimethylsiloxane monomers, was prepared by mixing the base polymer with its curing agent in a 10:1 weight ratio. The mixture was degassed and poured onto the epoxy mold and then cured at 65°C for 4 h. The cured PDMS was then carefully cut out and peeled off the mold. Individual mother-machine chips were cut out of the PDMS, and holes for the inlets and outlets were created using a biopsy puncher (0.75 mm diameter). The mother machine-like chips were cleaned with isopropanol, blow-dried with a nitrogen gun, and then cleaned with Scotch tape before bonding. Glass bottom dishes (40 mm diameter, 14026-20, from Ted Pella Inc., California, USA) were cleaned with isopropanol and blow-dried with a nitrogen gun. Finally, the PDMS chip and glass dish were plasma-treated (for 20 s at 60 W), immediately bonded, and baked at 65°C for 4 h. Chips were bonded the day before being used in the experiment.

Microfluidic setup

A simplified version of a previously described growth curve platform (Bakshi *et al*, 2021) was built using a peristaltic pump (T60-S2&WX10-14-H, Langer Instrument, USA) and an

in-house-built bubble trap. Platinum-cured silicon tubing (Masterflex™ L/S™ Platinum-Cured Silicone Precision Tubing, Tubing size 13, Fisher Scientific) was used to create the flow path. Blunt-end needles (1-1/2" Gauge 20, McMaster-Carr) were bent to create stable connections to the microfluidic chip. Before the experiment, the flow path was cleaned sequentially with 20% bleach, 20% ethanol, and Milli-Q water, each for 20 min. After cleaning, fresh M9gluCAAT medium supplemented with 0.8% Pluronic® F-108 was flown through the path for 10 min before connecting the loaded chip.

Microfluidics experiment and analysis

CJW7605 and CJW7668 strains were separately inoculated in 2 mL of M9gluCAAT medium supplemented with 0.08 % Pluronic® F-108 and grown overnight at 30°C with shaking at 220 rpm. An aliquot of the liquid cultures was then diluted 1:10,000 into 50 mL of M9gluCAAT medium in a 250-mL flask and returned to the shaker until reaching an OD of ~0.4. Three milliliters of each culture were spun at 6785 rcf and concentrated into 500 µL. The two cultures were mixed at this point and spun again at 6785 rcf to concentrate them to a final volume of ~30 µL. Cells were loaded into the microfluidic chip using gel-loading tips (Fisherbrand™ Gel-Loading Tips, 1-200µL, Fisher Scientific). The loaded chip was then spun at 500 g for 3 min using a modified version of the holder designed and shared by the Paulsson laboratory. The loaded chip was then connected to the flow path and placed inside the microscope incubator for 1 h to allow time for equilibration. After this time, fields of view were selected, and the batch culture of strain CJW2168 was inoculated using a 1:100000 dilution. Imaging was started immediately

following the inoculation of the culture, with a frame rate of 10 min for all the acquired channels.

In vitro phase separation experiments

To generate the presented phase diagram (Fig 6E), phase separation was assessed using varying concentrations of both glycogen (2.5 to 10 g/L) and 3 kDa PEG (8 to 30 mM). Samples were prepared in the IS buffer to a final volume of 50 µL in 200-µL Eppendorf tubes. For visualization, 0.05 µg/µL of FITC-ConA (Sigma-Aldrich C7642-2MG) was added to the appropriate glycogen volume prior to the addition of other components of the mixture. The appropriate volume of 3 kDa PEG was added last, and a 12-µL aliquot was immediately transferred to a 50 x 7mm glass bottom dish (PELCO) for imaging at 25°C.

To determine the minimal concentration of PEG/PEO that promotes glycogen phase separation, samples were prepared as described above with 9 g/L of glycogen. Increasing concentrations of each PEG (1.5 to 35 kDa) or PEO (100 kDa and 1 MDa) were tested in 50 µL mixtures. Each sample (12 µL) was imaged by phase contrast microscopy (100x Ph3 objective) to visually assess if glycogen condensates appeared. The smallest concentration at which the solutions transitioned from one phase to another was assigned as the minimal concentration. For PEO 1Mda, the minimal concentration required to drive phase separation was found to be above the overlap concentration (0.5% w/v) reported for this polymer (Smith *et al*, 2023), which marks the onset of “self-crowding”. Therefore, the hydrodynamic diameter of the polymer above this concentration could not

be determined using dynamic light scattering. Unless otherwise indicated, all experiments and imaging were conducted at 25°C.

For the fluorescent protein exclusion assay, glass-bottom dishes were cleaned using 1mL of 100% isopropanol, then washed twice with 90% ethanol, and allowed to dry completely. Dishes were then treated with Pluronic® F-108 (Sigma-Aldrich 542342-250G) to minimize fluorescent protein binding to the glass. Briefly, 200 µL of IS buffer supplemented with 0.1% w/v Pluronic® F-108 was pipetted into the dish and allowed to incubate for 1 h, followed by two washes with 200 µL of IS buffer. All remaining liquid was removed, and the dish was allowed to air dry completely. Mixtures were made to final concentrations of 10 g/L of glycogen, 1X IS buffer, 15 µM GFP (ThermoFisher A42613) or mCherry (Abcam AB199750), and 20 mM 3 kDa PEG as described above. Samples (12 µL) were imaged at 25°C, 30°C, and 37°C. For imaging, the focal plane was set on the surface of the glass to minimize background signal from the column of liquid around the condensates (Fig 5I), except for the images shown in Video EV6 for which images were taken as a z-stack (with 0.125 µm steps) above the glass surface. For the images shown in the figures, fluorescent image background subtraction was done using Fiji (Schindelin *et al*, 2012) and a sliding paraboloid with a rolling ball radius of 50 pixels.

MinD-GFP experiments

The CJW7872 strain was inoculated in 2 mL of M9gluCAAT medium and grown overnight at 30°C with shaking at 220 rpm. An aliquot of the culture was then diluted 1:10,000 into 50 mL of medium in a 250 mL flask and returned to the shaker. Samples were taken at OD 1.7, stained with DAPI as described above, and spotted onto agarose pads containing

transition-phase spent medium. Snapshots were acquired at time zero in the phase-contrast, DAPI, and FITC channels before the acquisition of a FITC time series (every 5 s for 95 s) to observe the MinD-GFP oscillations. A final snapshot series in all three channels was performed to correct for cell movement during the time series.

Fluorescence recovery after photobleaching

CJW7605 cells were inoculated in a 2-mL solution of M9gluCAAT and grown overnight at 30°C with shaking (220 rpm). An aliquot of the culture was then diluted 1:10,000 into 50 mL of medium in a 250-mL flask and returned to the shaker. Samples were taken at OD 1.7 and spotted onto agarose pads containing conditioned medium. Snapshots were taken before bleaching. For each field of view, an average of four cells were selected for FRAP analysis out of over 200 control cells. A disk (diameter = 5 pixels) was used to specify the region of interest for photobleaching and positioned at one of the cell poles, covering fully or partially the glycogen accumulation area. The regions of interest were bleached with a 405 nm laser at 25% power for 30 ms. Images were then acquired every 50 ms for 30 s following the bleaching.

Photobleaching correction was performed globally for each field of view using a custom Fiji macro (PhotoBleachCorrection.ijm). Briefly, the average fluorescence intensity across all control (non-bleached) cells was calculated for each time point and used to calculate a correction value centered on the fluorescence intensity at t = 0 (before photobleaching). The calculated correction factor for each time point was then applied to all pixels in the field of view. For each field of view, the photobleached cells and a randomly selected control cell were further analyzed.

After correction for photobleaching, FRAP analysis was performed using a custom MATLAB script (FRAP_Analysis.m). In brief, intensity profiles were extracted from the photobleached and non-photobleached regions using a circular region of interest of 5-pixels in diameter. Signal profiles were background-subtracted and normalized such that the first frame after photobleaching was zero and the maximum intensity after recovery was one. Each profile was then fitted by an exponential function to determine the half-time to maximal recovery. A total of 70 photobleached cells were analyzed.

Atomic force microscopy experiments

E. coli cells were immobilized on poly-L-lysine-coated glass-bottom Petri dishes. Fifty microliters of 0.01% poly-L-lysine were dropped on the glass-bottom Petri dish, air-dried for an hour, rinsed with Milli-Q water, and then dried with a nitrogen flow. A diluted cell suspension (500 µL) was dropped on the coated dishes and incubated at room temperature for 30 min before being rinsed with PBS five times to remove loose cells. Then, 2 mL of PBS were added to the dishes before AFM imaging. All AFM experiments were performed with a JPK NanoWizard V instrument (Bruker, USA) mounted on the inverted optical microscope Axio Observer (Zeiss, Germany). Depth-resolved stiffness map and stiffness tomography data were collected using the Quantitative Imaging (QI) mode with a force setpoint of 20 nN. SCANASYST-FLUID cantilevers (Bruker, USA) with a nominal spring constant of 0.35 N/m and a nominal tip radius of 20 nm were used in depth-resolved stiffness map and stiffness tomography experiments.

SCANASYST-FLUID+ cantilevers (Bruker, USA) with a nominal spring constant of 0.35 N/m and a nominal tip radius of 2 nm were used for stiffness measurements of the

intracellular content. AFM height images were first collected in QI mode with a minimal force setpoint (0.5 nN). Then, multiple force spectroscopies were collected on the designated area using the Contact mode. The force setpoint, the ramp size, and the tip velocity were set to 10 nN, 2 μm, and 2 μm/s, respectively. For each position, 8x8 force curves were recorded on a 50x50-nm^2 area. The spring constant and deflection sensitivity were calibrated prior to each experiment using the thermal noise method.

Atomic force microscopy data analysis

The depth-resolved stiffness map data were analyzed using the JPK NanoWizard V data processing software (Bruker, USA). The slope fit function in JPK NanoWizard V data processing software was applied. The fit range was 100% to 80% of the y channel (vertical deflection), which corresponds to 40-nm indentation depth from the end point of the curve. The stiffness tomography was generated using a customized Python code (AFM_stiffness_tomography_analysis.py), in which every 20-nm indentation segment after the contact point was analyzed for all force-distance curves along the cellular medial axis. The medial axis was extracted using code (Bivariate_medial_axis_estimation.py) from a previous study (Papagiannakis *et al*, 2025). The intracellular stiffness data were analyzed using a customized Python code (AFM_penetration_experiment_analysis.py), in which membrane rupture events were identified, and the slopes of the force-distance curves (the approach curves) were fitted after the rupture points. Only force-distance curves with membrane rupture events were analyzed.

DATA AVAILABILITY

Image analysis code and the newly trained segmentation models for images of *E. coli* cells on agarose pads and in the microfluidic device are available on the Jacobs-Wagner lab Github repository, along with the curation and training data generation code, (https://github.com/JacobsWagnerLab/published/tree/master/Thappeta_Canas-Duarte_et_al_2025). Images are available on Biostudies S-BIAD2088.

AUTHOR CONTRIBUTIONS

Y.T., S.J.C.-D., and C.J.-W. prepared the manuscript and conceptualized the study. W.G. and C.L. collected preliminary observations and data. YT, S.J.C-D. and C.J.-W. designed in vivo experiments. Y.T. and S.J.C.-D performed in vivo experiments. S.J.C.-D. and C.J.-W. designed in vitro experiments. S.J.C.-D. performed in vitro experiments and constructed the glycogen biosensor. S.J.C.-D. and Y.X. developed the analysis pipeline for the light microscopy experiments. G.H. produced the synthetic micrograph training data for the microfluidic experiments. S.J.C.-D performed and analyzed the microfluidic experiments. H.W. performed the AFM experiments and analyses. S.J.C.-D. and A.F. optimized the Omnipose segmentation model for analysis. S.J.C.-D. and Y.T. analyzed data. T.K. and L.C. performed and analyzed whole-cell NMR experiments. C.J.-W and L.C. provided supervision and funding acquisition. C.J.-W. provided project administration.

ACKNOWLEDGMENTS

We are grateful to Dr. Johan Paulsson for sharing unpublished strains, the epoxy cast of the microfluidic device, and the microfluidic centrifuge holder design used in this study.

We are also thankful to Dr. Somenath Bakshi for supervising Georgeos Hardo in generating the simulated bacterial images used to retrain Omnipose. We thank Drs. Suckjoon Jun and KC Huang for sharing published strains, and Dr. Sangjin Kim for generating a P1 transduction that generated strain CJW5685. We are thankful to Drs. Onn Brandman, KC Huang, and Jonas Cremer for valuable discussion. Finally, we express our gratitude to the Jacobs-Wagner laboratory for support, discussion, and critical reading of the manuscript. Part of this work was performed at the Stanford Nano Shared Facilities (SNSF), supported by the National Science Foundation under award ECCS-2026822. AFM experiments were performed at the Stanford University Cell Sciences Imaging Core Facility (RRID:SCR_017787). This research was supported in part by the Netherlands Organization for Scientific Research (NWO), Rubicon 2022-2 Science programme, 019.222EN.001 (to A.F.), the Biotechnology and Biological Sciences Research Council (BB/M011194/1 to G.H.), the Strategic Seed Fund from the School of Technology at the University of Cambridge (to G.H.), and the National Institutes of Health grant R01GM117278 (to L.C.). C.J.-W. is an investigator of the Howard Hughes Medical Institute.

DISCLOSURE AND COMPETING INTERESTS STATEMENT

The authors declare no competing interests.

REFERENCES

Åkerlund T, Nordstro¨m K, Nordstro¨m N & Bernander R (1995) Analysis of Cell Size and DNA Content in Exponentially Growing and Stationary-Phase Batch Cultures of Escherichia coli. *J Bacteriol* 177: 6791–6797

Alatossava T, Jütte H, Kuhn A & Kellenberger E (1985) Manipulation of intracellular magnesium content in polymyxin B nonapeptide-sensitized Escherichia coli by ionophore A23187. *J Bacteriol* 162: 413–419

Alberti S, Gladfelter A & Mittag T (2019) Considerations and Challenges in Studying Liquid-Liquid Phase Separation and Biomolecular Condensates. *Cell* 176: 419–434 doi:10.1016/j.cell.2018.12.035 [PREPRINT]

Alberti S & Hyman AA (2021) Biomolecular condensates at the nexus of cellular stress, protein aggregation disease and ageing. *Nat Rev Mol Cell Biol* 22: 196–213

Alberti S, Saha S, Woodruff JB, Franzmann TM, Wang J & Hyman AA (2018) A User's Guide for Phase Separation Assays with Purified Proteins. *J Mol Biol* 430: 4806–4820

Albi T & Serrano A (2016) Inorganic polyphosphate in the microbial world. Emerging roles for a multifaceted biopolymer. *World J Microbiol Biotechnol* 32: 27

Almagro G, Viale AM, Montero M, Rahimpour M, Muñoz FJ, Baroja-Fernández E, Bahaji A, Zúñiga M, González-Candelas F & Pozueta-Romero J (2015) Comparative genomic and phylogenetic analyses of gammaproteobacterial glg genes traced the origin of the Escherichia coli glycogen glgBXCAP operon to the last common ancestor of the sister orders Enterobacteriales and Pasteurellales. *PLoS One* 10

Alonso-Casajús N, Dauvillée D, Viale AM, Muñoz FJ, Baroja-Fernández E, Morán-Zorzano MT, Eydallin G, Ball S & Pozueta-Romero J (2006) Glycogen phosphorylase,

1229 the product of the glgP gene, catalyzes glycogen breakdown by removing glucose
1230 units from the nonreducing ends in Escherichia coli. *J Bacteriol* 188: 5266–5272
1231 Amselem E, Broadwater B, Hävermark T, Johansson M & Elf J (2023) Real-time single-
1232 molecule 3D tracking in E. coli based on cross-entropy minimization. *Nat Commun*
1233 14: 1–11
1234 Asakura S & Oosawa F (1954) On Interaction between Two Bodies Immersed in a
1235 Solution of Macromolecules. *J Chem Phys* 22: 1255–1256
1236 Asakura S & Oosawa F (1958) Interaction between particles suspended in solutions of
1237 macromolecules. *Journal of Polymer Science* 33: 183–192
1238 Azaldegui CA, Vecchiarelli AG & Biteen JS (2021) The emergence of phase separation
1239 as an organizing principle in bacteria. *Biophys J* 120: 1123–1138
1240 Azam TA, Hiraga S & Ishihama A (2000) Two types of localization of the DNA-binding
1241 proteins within the Escherichia coli nucleoid. *Genes to Cells* 5: 613–626
1242 Badrinarayanan A, Lesterlin C, Reyes-Lamothe R & Sherratt D (2012) The Escherichia
1243 coli SMC Complex, MukBEF, Shapes Nucleoid Organization Independently of DNA
1244 Replication. *J Bacteriol* 194: 4669–4676
1245 Bakshi S, Choi H, Mondal J & Weisshaar JC (2014) Time-dependent effects of
1246 transcription- and translation-halting drugs on the spatial distributions of the E
1247 scherichia coli chromosome and ribosomes. *Mol Microbiol* 94: 871–887
1248 Bakshi S, Leoncini E, Baker C, Cañas-Duarte SJ, Okumus B & Paulsson J (2021)
1249 Tracking bacterial lineages in complex and dynamic environments with applications
1250 for growth control and persistence. *Nature Microbiology 2021 6:6* 6: 783–791

1251 Bakshi S, Siryaporn A, Goulian M & Weisshaar JC (2012) Superresolution imaging of
1252 ribosomes and RNA polymerase in live Escherichia coli cells. *Mol Microbiol* 85: 21–
1253 38
1254 Baldwin WW, Myer R, Powell N, Anderson E & Koch AL (1995) Buoyant density of
1255 Escherichia coli is determined solely by the osmolarity of the culture medium. *Arch*
1256 *Microbiol* 164: 155–7
1257 Balleza E, Kim JM & Cluzel P (2018) Systematic characterization of maturation time of
1258 fluorescent proteins in living cells. *Nat Methods* 15: 47–51
1259 Banani SF, Lee HO, Hyman AA & Rosen MK (2017) Biomolecular condensates:
1260 Organizers of cellular biochemistry. *Nat Rev Mol Cell Biol* 18: 285–298
1261 Bates D & Kleckner N (2005) Chromosome and replisome dynamics in E. coli: Loss of
1262 sister cohesion triggers global chromosome movement and mediates chromosome
1263 segregation. *Cell* 121: 899–911
1264 Becker JW, Reeke GN, Cunningham BA & Edelman GM (1976) New evidence on the
1265 location of the saccharide-binding site of concanavalin A. *Nature* 259: 406–409
1266 Bennett AE, Rienstra CM, Auger M, Lakshmi K V. & Griffin RG (1995) Heteronuclear
1267 decoupling in rotating solids. *J Chem Phys* 103: 6951–6958
1268 Bezborodkina NN, Chestnova AY, Vorobev ML & Kudryavtsev BN (2018) Spatial
1269 Structure of Glycogen Molecules in Cells. *Biochemistry (Moscow)* 83: 467–482
1270 Boehm A, Arnoldini M, Bergmiller T, Röösli T, Bigosch C & Ackermann M (2016) Genetic
1271 Manipulation of Glycogen Allocation Affects Replicative Lifespan in E. coli. *PLoS*
1272 *Genet* 12

1273 Boeynaems S, Alberti S, Fawzi NL, Mittag T, Polymenidou M, Rousseau F, Schymkowitz
1274 J, Shorter J, Wolozin B, Van Den Bosch L, *et al* (2018) Protein Phase Separation: A
1275 New Phase in Cell Biology. *Trends Cell Biol* 28: 420–435
1276 Bourassa L & Camilli A (2009) Glycogen contributes to the environmental persistence
1277 and transmission of Vibrio cholerae. *Mol Microbiol* 72: 124–38
1278 Brandt F, Etchells SA, Ortiz JO, Elcock AH, Hartl FU & Baumeister W (2009) The Native
1279 3D Organization of Bacterial Polysomes. *Cell* 136: 261–271
1280 Bremer H & Dennis PP (2008) Modulation of Chemical Composition and Other
1281 Parameters of the Cell at Different Exponential Growth Rates. *EcoSal Plus* 3
1282 Bren A, Hart Y, Dekel E, Koster D & Alon U (2013) The last generation of bacterial growth
1283 in limiting nutrient. *BMC Syst Biol* 7: 27
1284 Buchanan RE (1918) Life Phases in a Bacterial Culture
1285 Castellana M, Hsin-Jung Li S & Wingreen NS (2016) Spatial organization of bacterial
1286 transcription and translation. *Proceedings of the National Academy of Sciences* 113:
1287 9286–9291
1288 Chai Q, Singh B, Peisker K, Metzendorf N, Ge X, Dasgupta S & Sanyal S (2014)
1289 Organization of Ribosomes and Nucleoids in Escherichia coli Cells during Growth
1290 and in Quiescence. *Journal of Biological Chemistry* 289: 11342–11352
1291 Chen YJ, Liu P, Nielsen AAK, Brophy JAN, Clancy K, Peterson T & Voigt CA (2013)
1292 Characterization of 582 natural and synthetic terminators and quantification of their
1293 design constraints. *Nature Methods 2013 10:7* 10: 659–664

1294 Cherepanov PP & Wackernagel W (1995) Gene disruption in Escherichia coli: TcR and
1295 KmR cassettes with the option of Flp-catalyzed excision of the antibiotic-resistance
1296 determinant. *Gene* 158: 9–14
1297 Cohan MC & Pappu R V. (2020) Making the Case for Disordered Proteins and
1298 Biomolecular Condensates in Bacteria. *Trends Biochem Sci* 45: 668–680
1299 Cutler KJ, Stringer C, Lo TW, Rappez L, Stroustrup N, Brook Peterson S, Wiggins PA &
1300 Mougous JD (2022) Omnipose: a high-precision morphology-independent solution
1301 for bacterial cell segmentation. *Nat Methods* 19: 1438–1448
1302 Datsenko KA & Wanner BL (2000) One-step inactivation of chromosomal genes in
1303 Escherichia coli K-12 using PCR products. *Proc Natl Acad Sci U S A* 97: 6640–5
1304 Devanand K & Selser JC (1991) Asymptotic behavior and long-range interactions in
1305 aqueous solutions of poly(ethylene oxide). *Macromolecules* 24: 5943–5947
1306 Diner EJ, Garza-Sánchez F & Hayes CS (2011) Genome Engineering Using Targeted
1307 Oligonucleotide Libraries and Functional Selection. In *Bone*, Williams JA (ed) pp 71–
1308 82. Totowa, NJ: Humana Press
1309 Dworkin J & Harwood CS (2022) Metabolic Reprogramming and Longevity in Quiescence.
1310 *Annu Rev Microbiol* 76: 91–111
1311 Elowitz MB, Surette MG, Wolf P-E, Stock JB & Leibler S (1999) Protein Mobility in the
1312 Cytoplasm of *Escherichia coli*. *J Bacteriol* 181: 197–203
1313 Erickson HP (2009) Size and shape of protein molecules at the nanometer level
1314 determined by sedimentation, gel filtration, and electron microscopy. *Biol Proced*
1315 *Online* 11: 32–51 doi:10.1007/s12575-009-9008-x [PREPRINT]

1316 Feijó Delgado F, Cermak N, Hecht VC, Son S, Li Y, Knudsen SM, Olcum S, Higgins JM,
1317 Chen J, Grover WH, *et al* (2013) Intracellular Water Exchange for Measuring the Dry
1318 Mass, Water Mass and Changes in Chemical Composition of Living Cells. *PLoS One*
1319 8: e67590
1320 Floc'h K, Lacroix F, Servant P, Wong Y-S, Kleman J-P, Bourgeois D & Timmins J (2019)
1321 Cell morphology and nucleoid dynamics in dividing Deinococcus radiodurans. *Nat*
1322 *Commun* 10: 3815
1323 Fung T, Kwong N, Van Der Zwan T & Wu M (2013) Residual Glycogen Metabolism in
1324 Escherichia coli is Specific to the Limiting Macronutrient and Varies During Stationary
1325 Phase
1326 Gangola P & Rosen BP (1987) Maintenance of intracellular calcium in Escherichia coli.
1327 *Journal of Biological Chemistry* 262: 12570–12574
1328 de Gennes PG & Witten TA (1980) *Scaling Concepts in Polymer Physics*. *Phys Today*
1329 33: 51–54
1330 Govons S, Vinopal R, Ingraham J & Preiss J (1969) Isolation of mutants of Escherichia
1331 coli B altered in their ability to synthesize glycogen. *J Bacteriol* 97: 970–972
1332 Gray WT, Govers SK, Xiang Y, Parry BR, Campos M, Kim S & Jacobs-Wagner C (2019)
1333 Nucleoid Size Scaling and Intracellular Organization of Translation across Bacteria.
1334 *Cell* 177: 1632-1648.e20
1335 Grossman TH, Kawasaki ES, Punreddy SR & Osburne MS (1998) Spontaneous cAMP-
1336 dependent derepression of gene expression in stationary phase plays a role in
1337 recombinant expression instability. *Gene* 209: 95–103

1338 Gründel M, Scheunemann R, Lockau W & Zilliges Y (2012) Impaired glycogen synthesis
1339 causes metabolic overflow reactions and affects stress responses in the
1340 cyanobacterium Synechocystis sp. PCC 6803. *Microbiology (United Kingdom)* 158:
1341 3032–3043
1342 Guerrero CR, Garcia PD & Garcia R (2019) Subsurface Imaging of Cell Organelles by
1343 Force Microscopy. *ACS Nano* 13: 9629–9637
1344 Hardo G, Noka M & Bakshi S (2022) Synthetic Micrographs of Bacteria (SyMBac) allows
1345 accurate segmentation of bacterial cells using deep neural networks. *BMC Biol* 20
1346 Hedge PJ & Spratt BG (1985) Resistance to β-lactam antibiotics by re-modelling the
1347 active site of an E. coli penicillin-binding protein. *Nature 1985 318:6045* 318: 478–
1348 480
1349 Henrissat B, Deleury E & Coutinho PM (2002) Glycogen metabolism loss: a common
1350 marker of parasitic behaviour in bacteria? *Trends in Genetics* 18: 437–440
1351 Hink MA, Griep RA, Borst JW, van Hoek A, Eppink MHM, Schots A & Visser AJWG (2000)
1352 Structural Dynamics of Green Fluorescent Protein Alone and Fused with a Single
1353 Chain Fv Protein. *Journal of Biological Chemistry* 275: 17556–17560
1354 Hoang AY, Azaldegui CA, Ghalmi M, Biteen JS & Vecchiarelli AG (2023) An experimental
1355 framework to assess biomolecular condensates in bacteria.
1356 Holme T, Laurent T, Palmstierna H, Magnéli A, Magnéli A, Pestmalis H & Åsbrink S (1957)
1357 On the Glycogen in Escherichia coli B; Variations in Molecular Weight during Growth.
1358 I. *Acta Chem Scand* 11: 757–762
1359 Holme T, Palmstierna H, Ulfvarson U, Stenhagen E & Thorell B (1956) Changes in
1360 Glycogen and Nitrogen-containing Compounds in Escherichia coli B during Growth

in Deficient Media. I. Nitrogen and Carbon Starvation. *Acta Chem Scand* 10: 578–586

Hyman AA, Weber CA & Jülicher F (2014) Liquid-liquid phase separation in biology. *Annu Rev Cell Dev Biol* 30: 39–58 doi:10.1146/annurev-cellbio-100913-013325 [PREPRINT]

Ingraham JL, Maaløe O & Neidhardt FC (1983) Growth of the bacterial cell Sunderland (Mass.) : Sinauer associates

Janel S, Popoff M, Barois N, Werkmeister E, Divoux S, Perez F & Lafont F (2019) Stiffness tomography of eukaryotic intracellular compartments by atomic force microscopy. *Nanoscale* 11: 10320–10328

Jensen KF (1993) The Escherichia coli K-12 'wild types' W3110 and MG1655 have an rph frameshift mutation that leads to pyrimidine starvation due to low pyrE expression levels. *J Bacteriol* 175: 3401–3407

Julius K, Weine J, Gao M, Latarius J, Elbers M, Paulus M, Tolan M & Winter R (2019) Impact of Macromolecular Crowding and Compression on Protein-Protein Interactions and Liquid-Liquid Phase Separation Phenomena. *Macromolecules* 52: 1772–1784

Khemici V, Poljak L, Luisi BF & Carpousis AJ (2008) The RNase E of Escherichia coli is a membrane-binding protein. *Mol Microbiol* 70: 799–813

Klotz A & Forchhammer K (2017) Glycogen, a major player for bacterial survival and awakening from dormancy. *Future Microbiol* 12: 101–104

Klotz A, Georg J, Bučinská L, Watanabe S, Reimann V, Januszewski W, Sobotka R, Jendrossek D, Hess WR & Forchhammer K (2016) Awakening of a Dormant

1384 Cyanobacterium from Nitrogen Chlorosis Reveals a Genetically Determined
1385 Program. *Current Biology* 26: 2862–2872
1386 Konopka MC, Sochacki KA, Bratton BP, Shkel IA, Record MT & Weisshaar JC (2009)
1387 Cytoplasmic Protein Mobility in Osmotically Stressed *Escherichia coli*. *J Bacteriol* 191:
1388 231–237
1389 Kubitschek HE, Baldwin WW & Graetzer R (1983) Buoyant density constancy during the
1390 cell cycle of Escherichia coli. *J Bacteriol* 155: 1027–1032
1391 Kubitschek HE & Friske JA (1986) Determination of bacterial cell volume with the Coulter
1392 Counter. *J Bacteriol* 168: 1466–1467
1393 Landgraf D, Okumus B, Chien P, Baker TA & Paulsson J (2012) Segregation of molecules
1394 at cell division reveals native protein localization. *Nat Methods* 9: 480–482
1395 Li XT, Jun Y, Erickstad MJ, Brown SD, Parks A, Court DL & Jun S (2016) tCRISPRi:
1396 tunable and reversible, one-step control of gene expression. *Scientific Reports 2016*
1397 *6:1* 6: 1–12
1398 Liu H, Wen J, Xiao Y, Liu J, Hopyan S, Radisic M, Simmons CA & Sun Y (2014) In situ
1399 mechanical characterization of the cell nucleus by atomic force microscopy. *ACS*
1400 *Nano* 8: 3821–8
1401 Liu Q, Li J, Zhang W, Xiao C, Zhang S, Nian C, Li J, Su D, Chen L, Zhao Q, *et al* (2021a)
1402 Glycogen accumulation and phase separation drives liver tumor initiation. *Cell* 184:
1403 5559-5576.e19
1404 Liu Q-H, Tang J-W, Wen P-B, Wang M-M, Zhang X & Wang L (2021b) From Prokaryotes
1405 to Eukaryotes: Insights Into the Molecular Structure of Glycogen Particles. *Front Mol*
1406 *Biosci* 8: 1–15

1407 Loferer-Krössbacher M, Klima J & Psenner R (1998) Determination of bacterial cell dry
1408 mass by transmission electron microscopy and densitometric image analysis. *Appl*
1409 *Environ Microbiol* 64: 688–94
1410 Lukatsky DB & Shakhnovich EI (2008) Statistically enhanced promiscuity of structurally
1411 correlated patterns. *Phys Rev E* 77: 020901
1412 Lutkenhaus J (2008) Min oscillation in bacteria. *Adv Exp Med Biol* 641: 49–61
1413 Lvov Y, Ariga K, Ichinose I & Kunitake T (1996) Molecular film assembly via layer-by-
1414 layer adsorption of oppositely charged macromolecules (linear polymer, protein and
1415 clay) and concanavalin A and glycogen. *Thin Solid Films* 284–285: 797–801
1416 Madsen NB (1963) The biological control of glycogen metabolism in Agrobacterium
1417 tumefaciens. *Can J Biochem Physiol* 41: 561–571
1418 Milo R (2013) What is the total number of protein molecules per cell volume? A call to
1419 rethink some published values. *BioEssays* 35: 1050–1055
1420 Mohapatra S & Weisshaar JC (2018) Functional mapping of the E. coli translational
1421 machinery using single-molecule tracking. *Mol Microbiol* 110: 262–282
1422 Mondal J, Bratton BP, Li Y, Yethiraj A & Weisshaar JC (2011) Entropy-based mechanism
1423 of ribosome-nucleoid segregation in E. coli Cells. *Biophys J* 100: 2605–2613
1424 Morcombe CR & Zilm KW (2003) Chemical shift referencing in MAS solid state NMR.
1425 *Journal of Magnetic Resonance* 162: 479–486
1426 Morita RY (1990) The starvation-survival state of microorganisms in nature and its
1427 relationship to the bioavailable energy. *Experientia* 46: 813–817

1428 Mulder EG, Deinema MH, van Veen WL & Zevenhuizen LPTM (1962) Polysaccharides,
1429 lipids and poly-β-hydroxybutyrate in microorganisms. *Recueil des Travaux*
1430 *Chimiques des Pays-Bas* 81: 797–809
1431 Neidhardt FC & Curtiss R (1996) Escherichia coli and Salmonella : cellular and molecular
1432 biology
1433 Nilsson M, Bülow L & Wahlund K-G (1997) Use of flow field-flow fractionation for the rapid
1434 quantitation of ribosome and ribosomal subunits inEscherichia coli at different protein
1435 production conditions. *Biotechnol Bioeng* 54: 461–467
1436 Nyström T (2004) Stationary-Phase Physiology. *Annu Rev Microbiol* 58: 161–181
1437 Nyström T & Kjelleberg S (1989) Role of Protein Synthesis in the Cell Division and
1438 Starvation Induced Resistance to Autolysis of a Marine Vibrio during the Initial Phase
1439 of Starvation. *Microbiology (N Y)* 135: 1599–1606
1440 Oak ASW, Bagchi A, Brukman MJ, Toth J, Ford J, Zheng Y, Nace A, Yang R, Hsieh J-C,
1441 Hayden JE, *et al* (2025) Wnt signaling modulates mechanotransduction in the
1442 epidermis to drive hair follicle regeneration. *Sci Adv* 11: eadq0638
1443 Paintdakhi A, Parry B, Campos M, Irnov I, Elf J, Surovtsev I & Jacobs-Wagner C (2016)
1444 Oufti: an integrated software package for high-accuracy, high-throughput quantitative
1445 microscopy analysis. *Mol Microbiol* 99: 767–77
1446 Papagiannakis A, Yu Q, Govers SK, Lin W-H, Wingreen NS & Jacobs-Wagner C (2025)
1447 Nonequilibrium polysome dynamics promote chromosome segregation and its
1448 coupling to cell growth in Escherichia coli. *Elife*

1449 Pelletier JF, Field CM, Coughlin M, Ryazanova L, Sonnett M, Wühr M & Mitchison TJ
1450 (2021) Glycogen-dependent demixing of frog egg cytoplasm at increased crowding.
1451 1–21
1452 Penedo M, Miyazawa K, Okano N, Furusho H, Ichikawa T, Alam MS, Miyata K, Nakamura
1453 C & Fukuma T (2021) Visualizing intracellular nanostructures of living cells by
1454 nanoendoscopy-AFM. *Sci Adv* 7: eabj4990
1455 Persson LB, Ambati VS & Brandman O (2020) Cellular Control of Viscosity Counters
1456 Changes in Temperature and Energy Availability. *Cell* 183: 1572-1585.e16
1457 Phillips LA, Hotham-Iglewski B & Franklin RM (1969) Polyribosomes of Escherichia coli:
1458 II. Experiments to determine the in vivo distribution of polysomes, ribosomes and
1459 ribosomal subunits. *J Mol Biol* 45: 23–38
1460 Pogliano J, Pogliano K, Weiss DS, Losick R & Beckwith J (1997) Inactivation of FtsI
1461 inhibits constriction of the FtsZ cytokinetic ring and delays the assembly of FtsZ rings
1462 at potential division sites
1463 Potma EO, De Boeij WP, Bosgraaf L, Roelofs J, Van Haastert PJM & Wiersma DA (2001)
1464 Reduced Protein Diffusion Rate by Cytoskeleton in Vegetative and Polarized
1465 Dictyostelium Cells. *Biophys J* 81: 2010–2019
1466 Preiss J (1984) Bacterial glycogen synthesis and its regulation. *Annu Rev Microbiol* 38:
1467 419–58
1468 Preiss J & Romeo T (1990) Physiology, Biochemistry and Genetics of Bacterial Glycogen
1469 Synthesis. In pp 183–238.
1470 Preiss J & Romeo T (1994) Molecular biology and regulatory aspects of glycogen
1471 biosynthesis in bacteria. *Prog Nucleic Acid Res Mol Biol* 47: 299–329

1472 Racki LR, Tocheva EI, Dieterle MG, Sullivan MC, Jensen GJ & Newman DK (2017)
1473 Polyphosphate granule biogenesis is temporally and functionally tied to cell cycle exit
1474 during starvation in Pseudomonas aeruginosa. *Proc Natl Acad Sci U S A* 114:
1475 E2440–E2449
1476 Roduit C, Sekatski S, Dietler G, Catsicas S, Lafont F & Kasas S (2009) Stiffness
1477 tomography by atomic force microscopy. *Biophys J* 97: 674–7
1478 Rolinson GN (1980) Effect of beta-lactam antibiotics on bacterial cell growth rate. *J Gen*
1479 *Microbiol* 120: 317–323
1480 Rostam N, Ghosh S, Chow CFW, Hadarovich A, Landerer C, Ghosh R, Moon HK,
1481 Hersemann L, Mitrea DM, Klein IA, *et al* (2023) CD-CODE: crowdsourcing
1482 condensate database and encyclopedia. *Nat Methods* 20: 673–676
1483 Sanamrad A, Persson F, Lundius EG, Fange D, Gynnå AH & Elf J (2014) Single-particle
1484 tracking reveals that free ribosomal subunits are not excluded from the Escherichia
1485 coli nucleoid. *Proc Natl Acad Sci U S A* 111: 11413–11418
1486 Schaefer J & Stejskal EO (1976) Carbon-13 Nuclear Magnetic Resonance of Polymers
1487 Spinning at the Magic Angle. *J Am Chem Soc* 98: 1031–1032
1488 Schavemaker PE, Śmigiel WM & Poolman B (2017) Ribosome surface properties may
1489 impose limits on the nature of the cytoplasmic proteome. *Elife* 6: 1–28
1490 Schindelin J, Arganda-Carreras I, Frise E, Kaynig V, Longair M, Pietzsch T, Preibisch S,
1491 Rueden C, Saalfeld S, Schmid B, *et al* (2012) Fiji: An open-source platform for
1492 biological-image analysis. *Nat Methods* 9: 676–682
1493 Schultz SG, Wilson NL & Epstein W (1962) Cation Transport in Escherichia coli. *Journal*
1494 *of General Physiology* 46: 159–166

1495 Sekar K, Linker SM, Nguyen J, Grünhagen A, Stocker R & Sauer U (2020) Bacterial
1496 Glycogen Provides Short-Term Benefits in Changing Environments. *Appl Environ*
1497 *Microbiol* 86
1498 Sharp KA (2015) Analysis of the size dependence of macromolecular crowding shows
1499 that smaller is better. *Proc Natl Acad Sci U S A* 112: 7990–7995
1500 Sherratt DJ (2003) Bacterial chromosome dynamics. *Science (1979)* 301: 780–785
1501 Shi H, Westfall CS, Kao J, Odermatt PD, Anderson SE, Cesar S, Sievert M, Moore J,
1502 Gonzalez CG, Zhang L, *et al* (2021) Starvation induces shrinkage of the bacterial
1503 cytoplasm. *Proc Natl Acad Sci U S A* 118: 2104686118
1504 Shih YL & Zheng M (2013) Spatial control of the cell division site by the Min system in
1505 Escherichia coli. *Environ Microbiol* 15: 3229–3239
1506 Shively JM (1974) Inclusion Bodies of Prokaryotes. *Annu Rev Microbiol* 28: 167–188
1507 Sigal N, Cattaneo J & Segel IH (1964) Glycogen accumulation by wild-type and uridine
1508 diphosphate glucose pyrophosphorylase-negative strains of Escherichia coli. *Arch*
1509 *Biochem Biophys* 108: 440–451
1510 Skurat A V., Segvich DM, Depaoli-Roach AA & Roach PJ (2017) Novel method for
1511 detection of glycogen in cells. *Glycobiology* 27: 416–424
1512 Smith WC, Qu H, Zheng K, Baek JH, Gao Y, Buehler PW, Feng X & Xu X (2023)
1513 Determining critical overlap concentration of polyethylene oxide to support excipient
1514 safety assessment of opioid products. *Int J Pharm* 632
1515 Strahl H, Turlan C, Khalid S, Bond PJ, Kebalo J-M, Peyron P, Poljak L, Bouvier M,
1516 Hamoen L, Luisi BF, *et al* (2015) Membrane Recognition and Dynamics of the RNA
1517 Degradosome. *PLoS Genet* 11: e1004961

1518 Strange RE, Dark FA & Ness AG (1961) The Survival of Stationary Phase Aerobacter
1519 aerogenes Stored in Aqueous Suspension. *J Gen Microbiol* 25: 61–76
1520 Stylianidou S, Brennan C, Nissen SB, Kuwada NJ & Wiggins PA (2016) SuperSegger:
1521 robust image segmentation, analysis and lineage tracking of bacterial cells. *Mol*
1522 *Microbiol* 102: 690–700
1523 Surovtsev I V. & Jacobs-Wagner C (2018) Subcellular Organization: A Critical Feature of
1524 Bacterial Cell Replication. *Cell* 172: 1271–1293
1525 Swaminathan R, Hoang CP & Verkman AS (1997) Photobleaching recovery and
1526 anisotropy decay of green fluorescent protein GFP-S65T in solution and cells:
1527 cytoplasmic viscosity probed by green fluorescent protein translational and rotational
1528 diffusion. *Biophys J* 72: 1900–1907
1529 Szatmári D, Sárkány P, Kocsis B, Nagy T, Miseta A, Barkó S, Longauer B, Robinson RC
1530 & Nyitrai M (2020) Intracellular ion concentrations and cation-dependent remodelling
1531 of bacterial MreB assemblies. *Sci Rep* 10: 12002
1532 Thomason LC, Costantino N & Court DL (2007) E. coli Genome Manipulation by P1
1533 Transduction. *Curr Protoc Mol Biol* 79
1534 Del Valle A, Torra J, Bondia P, Tone CM, Pedraz P, Vadillo-Rodriguez V & Flors C (2020)
1535 Mechanically Induced Bacterial Death Imaged in Real Time: A Simultaneous
1536 Nanoindentation and Fluorescence Microscopy Study. *ACS Appl Mater Interfaces* 12:
1537 31235–31241
1538 Wang L, Liu Q, Tan X, Wang Z, Wang M, Wise MJ, Li C, Ma C, Li E, Deng B, *et al* (2019a)
1539 Molecular Structure of Glycogen in Escherichia coli. *Biomacromolecules* 20: 2821–
1540 2829

1541 Wang L & Wise MJ (2011) Glycogen with short average chain length enhances bacterial
1542 durability. *Naturwissenschaften* 98: 719–729
1543 Wang M, Liu Q, Kang X, Zhu Z, Yang H, Xi X, Zhang X, Du Y, Guo M, Tang D, *et al* (2020)
1544 Glycogen Metabolism Impairment via Single Gene Mutation in the glgBXCAP Operon
1545 Alters the Survival Rate of Escherichia coli Under Various Environmental Stresses.
1546 *Front Microbiol* 11: 1–13
1547 Wang M, Liu Q, Li F, Tang J, Xiong X, Yang Y, Ju P, Wang Z, Gilbert RG & Wang L (2021)
1548 The dynamic changes of glycogen molecular structure in Escherichia coli BL21(DE3).
1549 *Carbohydr Polym* 259: 117773
1550 Wang P, Robert L, Pelletier J, Dang WL, Taddei F, Wright A & Jun S (2010) Robust
1551 Growth of Escherichia coli. *Current Biology* 20: 1099–1103
1552 Wang Z, Zhang G & Zhang H (2019b) Protocol for analyzing protein liquid–liquid phase
1553 separation. *Biophys Rep* 5: 1–9
1554 Wilson WA, Roach PJ, Montero M, Baroja-Fernández E, Muñoz FJ, Eydallin G, Viale AM
1555 & Pozueta-Romero J (2010) Regulation of glycogen metabolism in yeast and
1556 bacteria. *FEMS Microbiol Rev* 34: 952–985
1557 Woldringh CL, Mulder E, Valkenburg JAC, Wientjes FB, Zaritsky A & Nanninga N (1990)
1558 Role of the nucleoid in the toporegulation of division. *Res Microbiol* 141: 39–49
1559 Wu F, van Schie BGC, Keymer JE & Dekker C (2015) Symmetry and scale orient Min
1560 protein patterns in shaped bacterial sculptures. *Nat Nanotechnol* 10: 719–726
1561 Yoshioka K, Saito M, Oh K-B, Nemoto Y, Matsuoka H, Natsume M & Abe H (1996a)
1562 Intracellular Fate of 2-NBDG, a Fluorescent Probe for Glucose Uptake Activity, in
1563 *Escherichia coli* Cells. *Biosci Biotechnol Biochem* 60: 1899–1901

1564 Yoshioka K, Takahashi H, Homma T, Saito M, Oh K-B, Nemoto Y & Matsuoka H (1996b)
1565 A novel fluorescent derivative of glucose applicable to the assessment of glucose
1566 uptake activity of Escherichia coli. *Biochimica et Biophysica Acta (BBA) - General*
1567 *Subjects* 1289: 5–9
1568 Zevenhuizen LPTM (1966) Formation and function of the glycogen-like polysaccharide
1569 ofArthrobacter. *Antonie Van Leeuwenhoek* 32: 356–372
1570 Zhu Y, Fan Z, Wang R, Xie R, Guo H, Zhang M, Guo B, Sun T, Zhang H, Zhuo L, *et al*
1571 (2020) Single-Cell Analysis for Glycogen Localization and Metabolism in Cultured
1572 Astrocytes. *Cell Mol Neurobiol* 40: 801–812
1573
1574

FIGURE LEGENDS

Fig 1: Cellular features change as the cell density of the culture increases. A Growth curves of two independent cultures of strain CJW4677. The datapoints for the same culture have the same shape (spherical vs square). OD measurements were manually collected by spectrophotometry over time.

B Representative phase contrast images of DAPI-labeled cells in exponential (OD = 0.5), transition (OD = 2.0) and stationary phase (OD = 3.25). The magenta arrowhead indicates the site of cell constriction. The inset shows a zoomed of two cells in transition phase displaying cellular asymmetries in nucleoid and/or constriction positioning. The scale bars in the inset and larger field of view are 1 and 5 μm, respectively.

C Scatter plot of OD vs. mean cell area. Samples of different cultures of strain CJW4677 were collected at 35 different ODs (n > 500 cells for each OD) for cell imaging. The binned data for the indicated OD ranges are shown, with the mean describing the averaged mean value for cell samples from three OD values and error bars indicating the standard deviation. Grey, red, and blue shades indicate exponential, transition, and stationary phases, respectively.

D Same as panel C but for OD vs. mean nucleoid area.

E Same as panel C but for OD vs. mean number of nucleoids per cell.

F Same as panel C but for OD vs. fraction of cells with one nucleoid.

G Same as panel C but for OD vs. the fraction of constricting cells in the population.

H Same as panel C but for OD vs. mean division asymmetry, calculated by dividing the absolute distance of the division position from the cell center by cell length and averaging

across cells. This was done for cultures at ODs at which the fraction of dividing cells in the population was greater than 0.05.

I Kernel density plots of the relative nucleoid positioning for cells in exponential, transition, or stationary phases, determined by calculating the absolute distance between the nucleoid mid-point and cell center, normalized for cell length. Note that for cells with two nucleoids, their relative mid-points were averaged such that when the center of each nucleoid was positioned at the relative quarter cell positions, the mean mid-point was at the cell center (see schematic).

Fig 2: The localization pattern of cytoplasmic components changes in transition phase.

A Representative phase contrast and fluorescence images of DAPI-labeled CJW7325 cells expressing RplA-mCherry and msfGFP, along with corresponding cell signal intensity profiles. Cultures were in exponential phase (OD 0.14) or transition phase (OD 1.83), as indicated. Fluorescence intensity is indicated in arbitrary units (a.u.). Scale bar: 2 μm.

B Contour plots showing the normalized pole difference of msfGFP and RplA-mCherry signals in cells in exponential (top, n = 448) or transition (bottom, n = 2785) phase. The normalized pole difference of a fluorescent signal corresponds to the difference in this signal between pole regions divided by the average signal intensity across the cell. The contour lines represent the 0.167, 0.33, 0.5, 0.66, 0.83, and 1 kernel density envelopes of the data.

C Representative images of DAPI-stained CJW5685 cells expressing RNase E ΔMTS tagged with mCherry in exponential (OD = 0.1) or transition (OD = 1.3) phase, along with signal intensity profiles for the indicated (*) cell. Scale bar: 2 μm.

D Histograms of normalized pole difference of RNase E ΔMTS-mCherry in CJW5685 cells in exponential (OD = 0.1, n = 4732) or transition (OD = 1.7, n = 3110) phase.

E Timelapse sequence of a cell (CJW5159) expressing RplA-GFP and HupA-mCherry, with “N” and “O” indicating the new and old poles, respectively. Cells in exponential phase at OD ~0.5 were washed in spent medium from a transition-phase culture (OD = 2.63) and spotted on an agarose pad containing the same spent medium. The RplA-GFP images were scaled to reflect the 5-95% range of signal intensity for each image. The signal intensity profile is provided by the cell marked by an asterisk. Scale bar: 2 μm.

F Representative phase contrast and fluorescence images of a cephalexin-treated and DAPI-labeled CJW7325 cell carrying RplA-mCherry and msfGFP in transition phase, with the corresponding signal intensity profiles shown below. Fluorescence intensities are indicated in arbitrary units (a.u.). Scale bar: 5 μm.

G Same as panel F but highlighting a band of enriched msfGFP signal (purple arrowhead) in the region lacking DAPI staining (grey bracket). Scale bar: 5 μm.

H Phase contrast and fluorescence images of a CJW7326 cell carrying HupA-mCherry and msfGFP, along with the corresponding signal intensity profile. Scale bar: 1 μm.

Fig 3: Glycogen accumulation in transition phase drives intracellular rearrangement.

A Representative relative whole-cell ^{13}C CPMAS spectral overlays of WT cell extracts (strain CJW2168) from cultures in exponential vs. transition phase (top), purified bovine and mussel glycogen (middle), and WT vs. Δ*glgBXCAP* (CJW7537) cell extracts from transition-phase cultures (bottom). The dashed rectangle indicates the sugar carbon region of the spectrum.

B Representative fields of view of fluorescence images showing cells from co-cultures in transition phase. The top two fields of view show glycogen-producing cells (CJW7666) expressing mVenus and HupA-mCherry mixed with glycogen-devoid cells (CJW7667) expressing mSCFP3 and HupA-mCherry (Mix 1). The bottom fields of view illustrate glycogen-producing cells (CJW7665) expressing mSCFP3 and HupA-mCherry mixed with glycogen-devoid cells (CJW7668) expressing mVenus and HupA-mCherry (Mix 2). Scale bar: 10 μm. On the right side of the fields of view, the images of single cells (indicated by the single or double asterisks) show examples of the localization of mVenus (yellow), mSCFP3 (cyan), and HupA-mCherry (purple) for the relevant strain. Scale bar: 1 μm.

C Box plots showing the normalized (norm.) offset of the cell constriction site of the co-cultured WT and Δ*glgBXCAP* cells carrying either mVenus or mSCFP3 in exponential and transition phases. The horizontal lines and whiskers correspond to the median and the 1.5x interquartile range, respectively. The results shown correspond to the first replicate for Mix 1 and Mix 2. The results for two other biological replicates of each mix are shown in Fig EV4. The indicated P values were obtained using a two-sided Wilcoxon rank sum test.

D Same as panel C but for the normalized nucleoid position offset. The second and third biological replicates of Mix 1 and Mix 2 are shown in Fig EV5.

E Contour plots showing the normalized (Norm.) pole differences of msfGFP vs. the normalized pole differences of RplA-mCherry for exponential (top, OD = 0.065, n = 498) and transition-phase (bottom, OD = 1.2, n = 2807) cells of the glycogen-deficient strain Δ*glgBXCAP* (CJW7878). The normalized pole difference of a fluorescent signal corresponds to the difference in this signal between pole regions divided by the average signal intensity across the cell. The contour lines represent the 0.167, 0.33, 0.5, 0.66, 0.83, and 1 kernel density envelopes of the data.

F Histograms of the normalized pole difference of RNase E ΔMTS-mCherry for cells (strain CJW7877) in exponential (OD = 0.07, n = 2479) or transition (OD = 0.82, n = 3339) phase.

G Representative images of WT (CJW7606) and Δ*glgBXCAP* (CJW7607) cells in transition phase (OD 2.7) labeled with DAPI and expressing mScarlet-I and the glycogen sensor, along with the signal intensity profiles for the indicated (*) cells. Fluorescence intensities are indicated in arbitrary units (a.u.). Scale bar: 2 μm.

H Distributions of SCF values of the glycogen sensor vs. DAPI or mScarlet-I for glycogen-producing cells (n = 3591, CJW7606 in transition phase.

I Density contour plot showing the area difference of the glycogen sensor signal between the cell poles normalized by the cell area vs. the nucleoid position asymmetry in CJW7606 cells (n = 5794). The latter was calculated by determining the offset of the nucleoid mid-point from the cell center normalized to the cell length. The contour lines represent the

0.10, 0.2, 0.3, 0.4, 0.50, 0.6, 0.7, 0.8, and 0.9 probability envelopes of the data. Spearman correlation coefficient (ρ) is 0.748 (P-value = 0).

J Example phase contrast and fluorescence images of a DAPI-labeled CJW7606 cell carrying RplA-mCherry and the glycogen sensor. The cell was from a culture in transition phase following cephalexin treatment. Grey bracket indicates DNA-free region where glycogen accumulation (orange arrowheads) sandwiches a band of RplA-mCherry enrichment (purple arrowhead). Scale bar: 2 μm.

Fig 4. Preferential glycogen accumulation at the old cell pole through inheritance contributes to the asymmetry in nucleoid positioning.

A Schematic of the setup used in the microfluidic experiment. A waterbath shaker is used to grow a batch culture with controlled temperature (30°C) and shaking (200 rpm). Culture is first passed through a custom-built bubble trap and then through the microfluidics chip (mother machine) using a peristaltic pump. The large inset (dotted lines) shows a zoomed-in depiction of the microfluidic chip, with the culture flowing through the feeding channels and cells growing in the narrow trenches. The smaller inset shows an enlargement of the mother cell.

B Montage of a representative lineage of CJW7605 showing the overlay between the HupA-mCherry and glycogen sensor signals. Scale bar 2 μm.

C Plot showing the normalized glycogen sensor pole area over all observed generations. The solid line represents the mean across all tracked cell lineages (n = 130), while the shaded area indicates the 95% confidence interval.

D Scatter plot of the correlation between the normalized nucleoid offset and the normalized glycogen sensor pole area for all tracked lineages (n = 130) across all analyzed time points (color bar). Spearman correlation coefficient (ρ) is 0.826 (P value = 0).

E Plot showing the normalized nucleoid offset as a function of cell generations for the glycogen WT strain (CJW7605, n = 130 lineages) and the glycogen-deficient (Δ*glgBXCAP*) strain (CJW7668*,* n = 35 lineages*)*. The solid lines represent the means across all tracked cell lineages, while the shaded areas indicate the 95% confidence interval.

Fig 5: Asymmetry in glycogen accumulation creates cell size differences and asymmetric cell divisions.

A Density contour plot of the relative division position as a function of the nucleoid centroid position in dividing cells for transition-phase cells (strain CJW7666, n = 525). The values +0.5 and -0.5 represent the cell poles, while 0 corresponds to the cell center. Spearman correlation coefficient (ρ) for WT cells is 0.89 (P value = 0).

B Scatter plot showing the difference in cell area and the difference in the area occupied by the glycogen sensor between future daughter cells (strain CJW7606). Constricting cells (n = 365) were computationally divided into two future daughter cells based on the cell constriction position (illustrated in the inset). Spearman correlation coefficient (ρ) is 0.54 (P value = 1.28×10^{-27}).

C. Boxplots showing the area of exponential and transition-phase cells from WT (CJW7665 and CJW7666) and Δ*glgBXCAP* (CJW7667 and CJW7668) cultures carrying either mVenus (yellow) or mSCFP3 (cyan).

D Same as panel C but for the NC ratio.

E Same as panel C but for the total nucleoid area.

Fig 6. Mimicking intracellular conditions of crowding and ionic strength induces phase transition of glycogen into liquid condensates that partially exclude GFP.

A Plot showing dynamic light scattering (DLS) measurements of the particle diameter size for PEG and PEO polymers of different molecular weights in IS buffer. Samples were measured in triplicate for 300 s at 25°C with a 90-degree detection angle. The line indicates the empirical relation (hydrodynamic diameter ($\sigma_{PEG/PEO}$) = $0.029*MW_{PEG/PEO}^{(0.571\pm0.009)}$) determined by Devanand and Selser (1991).

B Phase contrast and ConA-FITC fluorescence images of representative fields of view showing a homogeneous distribution of glycogen (left), glycogen droplets (center), and collapsed glycogen aggregates (right) obtained with the indicated concentrations of 3 kDa PEG. All samples were made using the IS buffer and contained 9 g/L of glycogen. Scale bar: 10 μm.

C Example montages of glycogen condensates labeled with ConA-FITC undergoing fusion events over time. Scale bar: 3 μm.

D Fluorescence images of ConA-FITC-labeled glycogen condensates imaged at t ~ 3 min and t ~ 30 min after the addition of 3 kDa PEG. Scale bar: 10 μm

E Phase diagram of glycogen phases as a function of glycogen and 3 kDa PEG concentrations.

F Plot showing the minimal concentration required to drive droplet formation as a function of the average Stokes diameters for all tested PEG/PEO crowders. Phase separation was

determined by assessing the formation of droplets using phase contrast imaging. The average diameter for each PEG/PEO crowder corresponds to the measurements shown in (A).

G Phase contrast images of representative fields of view of glycogen (10 g/L) in IS buffer mixed with the indicated concentration and molecular weight of PEG or PEO (separately or combined). Scale bar: 10 μm.

H Phase contrast images of glycogen (10 g/L) and 3 kDa PEG (20 mM) mixtures in IS buffer before and after a two-fold dilution. For both conditions, imaging was performed within 1 min after mixing. Scale bar: 10 μm

I Phase contrast and GFP images of a representative field of view of glycogen (10g/L) in IS buffer mixed with GFP (15 μM) and 3 kDa PEG (20 mM). Scale bar: 10 μm.

Fig 7: Intracellular regions containing glycogen condensates are softer than those with protein aggregates and are comparable in stiffness to other cytoplasmic regions.

AFM experiments were performed on cells from three strains co-cultured to transition phase (ODs ranging between 1.5 and 1.7): CJW7798 overexpressing mTagBFP2 and accumulating protein aggregates at a cell pole, CJW7605 expressing the glycogen sensor to visualize glycogen condensates, and CJW7668 (Δ*glgBXCAP*) carrying free mVenus.

A Schematic of indentation-based subsurface AFM imaging with a cell containing a protein aggregate or a glycogen condensate.

B Two-dimensional depth-resolved stiffness maps (right) with the correlated fluorescence images (left) showing stiffness distributions for a representative cell with a protein

aggregate, a cell with accumulations of the fluorescent glycogen sensor (white arrows), or a cell without glycogen. Scale bar: 500 nm.

C Stiffness tomography showing the distribution of stiffness deviations along the indentation depth of cells with either a protein aggregate, glycogen condensates, or without glycogen. The stiffness deviation is the difference in stiffness between the stiffness value at each location and the median stiffness value across the cell length at the same indentation depth. Grey means no deviation.

D Schematic illustrating penetration-based stiffness measurements at targeted regions containing protein aggregates or glycogen condensates (labeled “On”) and at regions away from them (labeled “Off”).

E Plot showing the median stiffness of “On” and “Off” intracellular regions of either cells (n = 15) containing protein aggregates or cells (n = 16) with glycogen condensates, compared to cytoplasmic regions of glycogen-free cells (n = 13). Each dot represents the median stiffness of an individual cell obtained from 64 puncturing events (technical replicates). Data were collected over three independent experiments (biological replicates) with an average of ~ 5 cells per replicate.

SUPPLEMENTARY TABLES

Table EV1. Calculated concentrations of glycogen and proteins in *E. coli* under different growth conditions.

Glycogen			
Reported (mg/g dry weight)	Conversion (g/L)	Conditions	References
13	1.43	Exponential phase, 1% glucose in enriched medium (with yeast extract) at 37°C	(Govons *et al*, 1969; Preiss & Romeo, 1994)

2.5	8.25	Exponential phase, glucose minimal media at 37°C, 40 min division rate	(Ingraham *et al*, 1983)
2.8-4.4	9.24-14.52	Stationary phase, LB at 37°C	(Wang *et al*, 2019a)
19	20.9	Stationary phase, 1% glucose in enriched medium (with yeast extract) at 37°C	(Preiss & Romeo, 1994; Govons *et al*, 1969)
Proteins			
Reported	Conversion (mM)	Conditions	References
$2.35x10^6$ proteins per cell	4.48	Exponential phase, glucose minimal medium at 37°C, 40 min division rate	(Neidhardt & Curtiss, 1996)
0.24 g/mL	9.6-12	Calculated for proteins between 20 and 25 kDa	(Ingraham *et al*, 1983)

Glycogen and protein concentrations used in our study were derived from reported values for *E. coli* cells growing under different conditions. Glycogen concentrations from dry weight measurements (mg/g cells) were converted to wet weight values using a water content value of 70% (Bremer & Dennis, 2008; Feijó Delgado *et al*, 2013). To obtain the concentrations in g/L, we used a cell density of 1.1 g/mL (Kubitschek *et al*, 1983; Loferer-Krössbacher *et al*, 1998). To calculate the protein concentrations in mM from proteins per cell, we used a cell volume of 0.86 μm^3 (Kubitschek & Friske, 1986; Milo, 2013). To obtain the mM concentrations from g/mL, we used the indicated molecular weight range.

Table EV2. Calculated concentrations of ribosomes and polysomes used in this study.

Ribosomes per cell	Conditions	Cell volume (μm^3)	Estimated ribosome concentration (μM)	Estimated polysome concentration (μM)	References
3500	Stationary phase, LB at 37°C	1	5.8	1.16	(Nilsson *et al*, 1997)

15000	Exponential phase, M9gly at 37°C, 60 min doubling time	1	24.9	4.98	(Bremer & Dennis, 2008)
61000	Exponential phase, M9gluCAA at 37°C, 24 min doubling time	3.5	28.9	5.79	(Bremer & Dennis, 2008)

Concentrations were determined from the reported numbers of ribosomes per cell using the Avogadro constant to calculate the number of moles per cell, then dividing by the reported cell volume values indicated (Floc'h *et al*, 2019; Kubitschek & Friske, 1986). For polysomes, an active fraction of 0.8 percent was used (Bremer & Dennis, 2008) and a polysome was assumed to consist of four ribosomes (Brandt *et al*, 2009).

Table EV3. Conditions that resulted in fluorescent protein exclusion from glycogen droplets in vitro.

PEG/PEO (MW)	PEG/PEO concentration	Temperature (°C)	FP	Buffer	FP exclusion
1.5 kDa	60 mM	30	GFP	IS	Yes
3 kDa	20 mM	25	GFP	IS	Yes
3 kDa	20 mM	30	GFP	IS	Yes
3 kDa	20 mM	37	GFP	IS	Yes
3 kDa	20 mM	25	GFP	IS without $MgCl_2$	Yes
3 kDa	20 mM	25	mCherry	IS	Yes
4 kDa	15 mM	25	GFP	IS	Yes
4 kDa	15 mM	30	GFP	IS	Yes
4 kDa	15 mM	37	GFP	IS	Yes
8 kDa	3 mM	25	GFP	IS	Yes
8 kDa	3 mM	30	GFP	IS	Yes
20 kDa	750 µM	30	GFP	IS	Yes
100 kDa	20 µM	25	GFP	IS	Yes
1 MDa	10 µM	25	GFP	IS	Yes

Summary of the assays performed for testing the exclusion of fluorescent proteins (FPs) by glycogen liquid condensates. FP exclusion was detected by phase contrast and fluorescence imaging. For all assays, 10 g/L of glycogen and 15 µM of the FP (GFP or mCherry) were used.

1823 **Table EV4: Strain construction table**

Identifier	Genotype	Source or construction method
CJW5685	MG1655 *rne*::*rneΔMTS-mcherry*	*rne*::*rne-mCherry-FRT-cat-FRT* from parent strain of Kti162 (Strahl *et al*, 2015) was moved into MG1655 by P1 transduction. Colonies were screened for chloramphenicol resistance and mCherry fluorescence. The resistance cassette was excised by transiently equipping this strain with plasmid pCP20 expressing the Flp site-specific recombinase (Cherepanov & Wackernagel, 1995).
CJW7083	MG1655 *attB*::P_{proC}-*msfGFP*-FRT-*kan*-FRT	pKD13 was amplified from plasmid pKD13-msfGFP (Gray *et al*, 2019) using primers YP32 and YP33, with YP32 encoding a transcriptional terminator sequence. *msfGFP* was also amplified from this plasmid using YP34 and YP35. Constitutive synthetic promoter P_{proC} was amplified from CJW7006 using primers YP36 and YP37, with YP37 also encoding the ribosome binding site L3S1P13 (Chen *et al*, 2013), linker sequence and start codon. These pieces were assembled using Gibson assembly. The construct was then integrated into the chromosome of MG1655 at the *attB* site using lambda red recombination.
CJW7275	MG1655 *attB*::P_{proC}-*msfGFP*	The kanamycin resistance cassette of CJW7083 was excised by transiently equipping this strain with plasmid pCP20, expressing the Flp site specific recombinase (Cherepanov & Wackernagel, 1995).
CJW7325	MG1655 *rplA*::*rplA-mCherry attB*::P_{proC}-*msfGFP*	*attB*::PproC-msfGFP - KAN from CJW7083 was moved into CJW7324 by P1 transduction. Colonies were screened for kanamycin resistance and GFP fluorescence. The kanamycin resistance cassette was excised by transiently equipping this strain with plasmid pCP20, expressing the Flp site specific recombinase (Cherepanov & Wackernagel, 1995).

CJW7326	MG1655 *attB*::P_{proC}-*msfGFP hupA*::*hupA-mCherry*	*hupA-mCherry*-FRT-*kan*-FRT from CJW5158 (Gray *et al*, 2019) was moved into CJW7275 by P1 transduction. Colonies were screened for kanamycin resistance and mCherry fluorescence. The kanamycin resistance cassette was excised by transiently equipping this strain with plasmid pCP20, expressing the Flp site specific recombinase (Cherepanov & Wackernagel, 1995).
CJW7485	MG1655 *rplA*::*rplA-mCherry*/pBAD-GFP(-30)	CJW7324 was transformed with plasmid pBAD-GFP(-30).
CJW7486	MG1655 *rplA*::*rplA-mCherry*/pBAD-GFP(-7)	CJW7324 was transformed with plasmid pBAD-GFP(-7).
CJW7487	MG1655 *rplA*::*rplA-mCherry*/pBAD-GFP(0)	CJW7324 was transformed with plasmid pBAD-GFP(0).
CJW7488	MG1655 *rplA*::*rplA-mCherry*/pBAD-GFP(+7)	CJW7324 was transformed with plasmid pBAD-GFP(+7).
CJW7489	MG1655 *rplA*::*rplA-mCherry*/pBAD-GFP(+11a)	CJW7324 was transformed with plasmid pBAD-GFP(+11a).
CJW7490	MG1655 *rplA*::*rplA-mCherry*/pBAD-GFP(+11b)	CJW7324 was transformed with plasmid pBAD-GFP(+11b).
CJW7491	MG1655 *rplA*::*rplA-mCherry*/pBAD-GFP(+15)	CJW7324 was transformed with plasmid pBAD-GFP(+15).
CJW7492	MG1655 *rplA*::*rplA-mCherry*/pBAD-GFP(+25)	CJW7324 was transformed with plasmid pBAD-GFP(+25).
CJW7537	MG1655 Δ*glgBXCAP*-FRT-*kan*-FRT	The glycogen operon was replaced with a kanamycin cassette using lambda red from the plasmid pSIM6 (Diner *et al*, 2011) using gene block gb_1. Candidate colonies we confirmed by PCR.
CJW7587	MG1655 Δ*glgBXCAP*	The kanamycin resistance cassette from CJW7537 was excised by transiently equipping this strain with plasmid pCP20, expressing the Flp site specific recombinase (Cherepanov & Wackernagel, 1995).

CJW7588	MG1655 *lacY(A177C) araFGH*::*spec* Δ*lacI* Δ*araE araBAD*::*dCas9 galM <PBBa-J23119-sgRNA(ftsZ)-(S. pyogenes* terminator*)-(rrnB* terminator*)> gmpA attB*::P_{proC}*-msfGFP*	*attB*::P_{proC}*-msfGFP*-FRT-*kan*- FRT from CJW7083 was moved into SJ_XTL229 by P1 transduction. Colonies were screened for kanamycin resistance and GFP fluorescence. The kanamycin resistance cassette was excised by transiently equipping this strain with plasmid pCP20, expressing the Flp site specific recombinase (Cherepanov & Wackernagel, 1995).
CJW7601	MG1655 Tn7::P_{tac}-*GFPmut3-CBM20* FRT-*cat*-FRT	Plasmid pNDL-1-P_{tac}-GFPmut3-CBM20 FRT-CmR-FRT was transformed into MG1655. Colonies were screened for ampicillin resistance at 30°C. Integration was then carried out by incubating at 37°C and selecting for chloramphenicol resistance
CJW7604	MG1655 *ΔglgBXCAP* Tn7::P_{tac}-*GFPmut3-CBM20*-FRT-*cat*-FRT	Plasmid pNDL-1-P_{tac} -GFPmut3-CBM20 FRT-CmR-FRT was transformed into CJW7587. Colonies were screened for ampicillin resistance at 30°C. Integration was then carried out by incubating at 37°C and selecting for chloramphenicol resistance
CJW7605	MG1655 Tn7::P_{tac}-*GFPmut3-CBM20* FRT-*cat*-FRT *hupA*::*hupA-mCherry FRT-kan-FRT*	*hupA-mCherry*-FRT-*kan*-FRT from CJW5158 (Gray *et al*, 2019) was moved into CJW7601 by P1 transduction
CJW7606	MG1655 Tn7:: P_{tac} -*GFPmut3-CBM20*-FRT-*cat*-FRT	CJW7601 was transformed with pEB2-mScarlet-I.
CJW7607	MG1655 Δ*glgBXCAP* Tn7::P_{tac}-*GFPmut3-CBM20* FRT-*cat* -FRT	CJW7604 was transformed with pEB2-mScarlet-I.
CJW7660	MG1655 *hupA*::*hupA-mCherry*	*hupA-mCherry*-FRT-*kan*-FRT from CJW5158 (Gray *et al*, 2019) was moved into MG1655 by P1 transduction. Colonies were screened for kanamycin resistance and mCherry fluorescence. The kanamycin resistance cassette was excised by transiently equipping this strain with plasmid pCP20, expressing the Flp site-specific recombinase (Cherepanov & Wackernagel, 1995).

CJW7661	MG1655 Δ*glgBXCAP hupA*::*hupA-mCherry*	*hupA-mCherry*-FRT-*kan*-FRT from CJW5158 (Gray *et al*, 2019) was moved into CJW7587 by P1 transduction. Colonies were screened for kanamycin resistance and mCherry fluorescence. The kanamycin resistance cassette was excised by transiently equipping this strain with plasmid pCP20, expressing the Flp site specific recombinase (Cherepanov & Wackernagel, 1995).
CJW7665	MG1655 *hupA*::*hupA-mCherry* Tn7:: P_{RpsL}-*mSCFP3*-FRT-*kan*-FRT	Tn7:: P_{RpsL}-*mSCFP3*-FRT-*kan*-FRT from JP1456 was moved into CJW7660 by P1 transduction. Colonies were screened for kanamycin resistance and CFP fluorescence.
CJW7666	MG1655 *hupA*::*hupA-mCherry* Tn7:: P_{RpsL}-*mVenus*-FRT-*kan*-FRT	Tn7:: P_{RpsL}-*mVenus*-FRT-*kan*- FRT from JP1457 was moved into CJW7660 by P1 transduction. Colonies were screened for kanamycin resistance and YFP fluorescence.
CJW7667	MG1655 Δ*glgBXCAP hupA*::*hupA-mCherry* Tn7:: P_{Rps}-*mSCFP3*-FRT-*kan*-FRT	Tn7:: P_{Rps}-*mSCFP3*-FRT-*kan*-FRT from JP1456 was moved into CJW7661 by P1 transduction. Colonies were screened for kanamycin resistance and CFP fluorescence.
CJW7668	MG1655 Δ*glgBXCAP hupA*::*hupA-mCherry* Tn7:: P_{Rps}-*mVenus*-FRT-*kan*-FRT	Tn7::P_{Rps}-*mVenus*-FRT-*kan*- FRT from JP1457 was moved into CJW7661 by P1 transduction. Colonies were screened for kanamycin resistance and YFP fluorescence.
CJW7718	MG1655 Δ*glgBXCAP* /pEB2-mScarlet-I	CJW7587 was transformed with plasmid pEB2-mScarlet-I from AddGene #104007 (Balleza *et al*, 2018)
CJW7872	MG1655 *ΔminD minE::sfgfp-minD minE::frt kanR frt*	*ΔminD minE::sfgfp-minD minE::frt kanR frt* was moved into MG1655 by P1 transduction from FW1537 (Wu *et al*, 2015)
CJW7877	MG1655 Δ*glgBXCAP rne*::*rneΔMTS-mCherry*	Δ*glgBXCAP*-FRT-*kan*-FRT was moved into CJW5685 by P1 transduction from CJW7537
CJW7878	MG1655 Δ*glgBXCAP rplA*::*rplA-mCherry attB*::P_{proC}-*msfGFP*	Δ*glgBXCAP*-FRT-*kan*-FRT was moved into CJW7325 by P1 transduction from CJW7537

1824

1825 **Table EV6. Oligos used in this study.**

Identifier	Sequence (5' to 3')
gb_1	TCAATAATACCGGCAAGTCCGACACCCAGCATGGCAATAACCACCGCCAAA AATTGCGCCAGTATGGGGATGCCGAAAAAAGTCATTACCAGCGAGGTCAAA ATCCATTTTCTGTTTTGCATTATTCTTTCCATTCTTTTTGAATGGTGAAATTAT ACTCCCCGAGTCCCCTTGCCCCTTCTGGACACTTTTCCGAAATGATGGCGG AAAAAAACGGGACCCTTTGGCCCCGTTCTATTTATTGGTGAACGTGTAGGC TGGAGCTGCTTCGAAGTTCCTATACTTTCTAGAGAATAGGAACTTCGGAATA GGAACTTCAAGATCCCCTTATTAGAAGAACTCGTCAAGAAGGCGATAGAAG GCGATGCGCTGCGAATCGGGAGCGGCGATACCGTAAAGCACGAGGAAGC GGTCAGCCCATTCGCCGCCAAGCTCTTCAGCAATATCACGGGTAGCCAAC GCTATGTCCTGATAGCGGTCCGCCACACCCAGCCGGCCACAGTCGATGAA TCCAGAAAAGCGGCCATTTTCCACCATGATATTCGGCAAGCAGGCATCGCC ATGGGTCACGACGAGATCCTCGCCGTCGGGCATGCGCGCCTTGAGCCTG GCGAACAGTTCGGCTGGCGCGAGCCCCTGATGCTCTTCGTCCAGATCATC CTGATCGACAAGACCGGCTTCCATCCGAGTACGTGCTCGCTCGATGCGAT GTTTCGCTTGGTGGTCGAATGGGCAGGTAGCCGGATCAAGCGTATGCAGC CGCCGCATTGCATCAGCCATGATGGATACTTTCTCGGCAGGAGCAAGGTG AGATGACAGGAGATCCTGCCCCGGCACTTCGCCCAATAGCAGCCAGTCCC TTCCCGCTTCAGTGACAACGTCGAGCACAGCTGCGCAAGGAACGCCCGTC GTGGCCAGCCACGATAGCCGCGCTGCCTCGTCCTGCAGTTCATTCAGGGC ACCGGACAGGTCGGTCTTGACAAAAAGAACCGGGCGCCCCTGCGCTGACA GCCGGAACACGGCGGCATCAGAGCAGCCGATTGTCTGTTGTGCCCAGTCA TAGCCGAATAGCCTCTCCACCCAAGCGGCCGGAGAACCTGCGTGCAATCC ATCTTGTTCAATCATGCGAAACGATCCTCATCCTGTCTCTTGATCAGATCTT GATCCCCTGCGCCATCAGATCCTTGGCGGCAAGAAAGCCATCCAGTTTACT TTGCAGGGCTTCCCAACCTTACCAGAGGGCGCCCCAGCTGGCAATTCCGG TTCGCTTGCTGTCCATAAAACCGCCCAGTCTAGCTATCGCCATGTAAGCCC ACTGCAAGCTACCTGCTTTCTCTTTGCGCTTGCGTTTTCCCTTGTCCAGATA GCCCAGTAGCTGACATTCATCCGGGGTCAGCACCGTTTCTGCGGACTGGC TTTCTACGTGTTCCGCTTCCTTTAGCAGCCCTTGCGCCCTGAGTGCTTGCG GCAGCGTGAGCTTCAAAAGCGCTCTGAAGTTCCTATACTTTCTAGAGAATA GGAACTTCGGCTTGTCTTCCTGTTTTATTGTGTCACCCCATCCAATTGGATT TTTGACTTCTGGTTGTGACATTTTTTTGACCTGAACGGCGCAGCACTCTGTG CATCCTCTCTGCGTCGTCCTCACTTCAGGTAAGGCTGTGAATACTCATGTA TTCAGCCACCCTTAAAGAATAGCCAATGCTCTATTTAACTCCCGGTAAATCA TGAAACATCTGCGCTTACTCCTGTATTACGCACTAACAGGGGCGGCATCGC GCCCCAGATTTAATGAATAAAGATTACGCCAGTT
gb_2	CACCGAATTCCCCGGGGGGGGACAAGTTTGTACAAAAAAGCAGGCTTACGA CATCATAACGGTTCTGGCAAATATTCTGAAATGAGCTGTTGACAATTAATCA TCGGCTCGTATAATGTGTGGAATTGTGAGCGGATAACAATTTCACACAGGA AACAGAATATGAGTAAAGGAGAAGAACTTTTCACTGGAGTTGTCCCAATTCT TGTTGAATTAGATGGTGATGTTAATGGGCACAAATTTTCTGTCAGTGGAGA GGGTGAAGGTGATGCAACATACGGAAAACTTACCCTTAAATTTATTTGCACT ACTGGAAAACTACCTGTTCCATGGCCAACACTTGTCACTACTTTCGGTTATG GTGTTCAATGCTTTGCGAGATACCCAGATCATATGAAACAGCATGACTTTTT

	CAAGAGTGCCATGCCCGAAGGTTATGTACAGGAAAGAACTATATTTTTCAA AGATGACGGGAACTACAAGACACGTGCTGAAGTCAAGTTTGAAGGTGATAC CCTTGTTAATAGAATCGAGTTAAAAGGTATTGATTTTAAAGAAGATGGAAAC ATTCTTGGACACAAATTGGAATACAACTATAACTCACACAATGTATACATCA TGGCAGACAAACAAAAGAATGGAATCAAAGTTAACTTCAAAATTAGACACAA CATTGAAGATGGAAGCGTTCAACTAGCAGACCATTATCAACAAAATACTCCA ATTGGCGATGGCCCTGTCCTTTTACCAGACAACCATTACCTGTCCACACAA TCTAAGCTTTCGAAAGATCCCAACGAAAAGAGAGACCACATGGTCCTTCTT GAGTTTGTAACAGCTGCTGGGATTACACATGGCATGGATGAACTATACAAA AGCGATTTCATGCCTGCCGGTTCTCAACAGGTTAGCGTTCGTTTTCAGGTA CACTACGTCACTTCCACCGACGTTCAGTTTATTGCAGTGACCGGCGATCAC GAGTGCCTGGGCCGCTGGAACACGTACATCCCTCTGCACTACAACAAAGA CGGTTTCTGGTCCCACAGCATCTTTCTGCCGGCGGATACCGTTGTGGAGT GGAAATTTGTTCTGGTTGAAAACGGTGGCGTTACGCGTTGGGAGGAATGTT CCAACCGTTTCCTGGAAACCGGTCACGAAGATAAGGTAGTTCACGCGTGG TGGGGTATCCATTAAATGTCCAGACCTGCAGGCATGCAAGCTCTAGTTGGA TTCTCACCAATAAAAAACGCCCGGCGGCAACCGAGCGTTCTGAACAAATCC AGATGGAGTTCTGAGGTCATTACTGGATCTATCAACAGGAGTCCAAGCGAG CGAATTCTGCAGGTGTTAATTCAGGAGCATTGTTATCAGACCAAATATGTGT AGGCTGGAGCTGCTTCGAAGTTCCTATACTTTCTAGAGAATAGGAACTTCG GAATAGGAACTTCTTATCAAAAAGGATCTTCACCTAGATCCTTTTAAATTAAA AATGAAGTTTTAAATCAATCTAAAGTATATATGAGTAAACTTGGTCTGACAG CTCGAGGCGCTCGATATCAAATTACGCCCCGCCCTGCCACTCATCGCAGT ACTGTTGTAATTCATTAAGCATTCTGCCGACATGGAAGCCATCACAAACGG CATGATGAACCTGAATCGCCAGCGGCATCAGCACCTTGTCGCCTTGCGTAT AATATTTGCCCATGGTGAAAACGGGGGCGAAGAAGTTGTCCATATTGGCCA CGTTTAAATCAAAACTGGTGAAACTCACCCAGGGATTGGCTGAGACGAAAA ACATATTCTCAATAAACCCTTTAGGGAAATAGGCCAGGTTTTCACCGTAACA CGCCACATCTTGCGAATATATGTGTAGAAACTGCCGGAAATCGTCGTGGTA TTCACTCCAGAGCGATGAAAACGTTTCAGTTTGCTCATGGAAAACGGTGTA ACAAGGGTGAACACTATCCCATATCACCAGCTCACCGTCTTTCATTGCCAT ACGAAATTCCGGATGAGCATTCATCAGGCGGGCAAGAATGTGAATAAAGG CCGGATAAAACTTGTGCTTATTTTTCTTTACGGTCTTTAAAAAGGCCGTAAT ATCCAGCTGAACGGTCTGGTTATAGGTACATTGAGCAACTGACTGAAATGC CTCAAAATGTTCTTTACGATGCCATTGGGATATATCAACGGTGGTATATCCA GTGATTTTTTTCTCCATTTTAGCTTCCTTAGCTCCTGAAAATCTCGATAACTC AAAAAATACGCCCGGTAGTGATCTTATTTCATTATGGTGAAAGTTGGAACCT CTTACGTGCCCGATCAACTCGAGTGCCACCTGACGTCTAAGAAACCATTAT TATCATGACATTAACCTATAAAAATAGGCGTATCACGAGGCAGAATTTCAGA TAAAAAAAATCCTTAGCTTTCGCTAAGGATGATTTCTGGAAGCGCTCTGAAG TTCCTATACTTTCTAGAGAATAGGAACTTCGTACCCAGCTTTCTTGTACAAA GTGGTCCCCAAGCTTCTGCAGAGCT
YP32	TACTAGAGGACGAACAATAAGGCCTCCCTAACGGGGGGCCTTTTTTATTGA TAACAAAAGTGTAGGCTGGAGCTGCTTCG
YP33	AATCGCTCAAGACGTGTAATGCTGCAATC
YP34	TCAAAAGGCGAAGAACTTTTTACCG

YP35	TAGGGAGGCCTTATTGTTCGTCCTCTAGTATTATTTATACAATTCATCCATTC CATGAGTGA
YP36	CCAGTGCCAAGCTTGCATGCAGATTGCAGCATTACACGTCTTGAGCGATTC ACAGCTAACACCACGTCG
YP37	TACACCGGTAAAAAGTTCTTCGCCTTTTGACATCTAGTATTCTCCTCTTTCT CTAGTAAAAGTTAAACAAAATTATTTGTAGAGGGAAAC

1826

1827

EXPANDED VIEW FIGURE LEGENDS

Fig EV1: Localization of various cytoplasmic probes in cells in transition phase.

A Representative fluorescence images of DAPI-stained *E. coli* cells expressing different ribosomal protein fusions in transition phase: RplA-GFP (CJW4677), RplA-msfGFP (CJW7020), and RpsB-msfGFP (CJW7021). Arrowheads indicate cell areas of ribosome signal depletion. Scale bar: 2 µm.

B Representative fluorescence image of DAPI-stained *E. coli* cells (CJW7006) expressing mScarlet-I in transition phase. Arrowheads indicate cell areas of mScarlet-I depletion. Scale bar: 2 µm.

C Representative fluorescence images of DAPI-stained *E. coli* expressing RplA-mCherry as well as free fluorescent GFP variants with the following net surface charges (strain name): -30 (CJW7485), -7 (CJW7486), 0 (CJW7487), +7 (CJW7488), +11a (CJW7489), +11b (CJW7490), +15 (CJW7491), and +25 (CJW7492). For GFP with a net surface charge +11, ‘a’ and ‘b’ refer to variations in the distribution of the charge on the protein surface (Schavemaker *et al*, 2017). Cells were grown in M9gluCAAT and supplemented with 0.4% arabinose to induce GFP expression. Arrowheads indicate cell areas depleted of the GFP variant. Scale bar: 2 µm.

D Fluorescence images of representative DAPI- and RNASelect-labeled *E. coli* cells (CJW7324) in exponential (OD 0.30) and transition (OD 1.72) phase. Also shown are the corresponding fluorescence signal profiles for the indicated (*) cells. Arrowheads indicate areas depleted of RNASelect signal. Scale bar: 2 µm.

Fig EV2: Assessment of the potential effects of membrane retraction and cell division on the localization of cytoplasmic probes in transition-phase cells

A Microscopy images of MitoTracker Green-labeled cells (CJW7324) expressing RplA-mCherry. Samples were obtained from cultures in either exponential or transition phase. Fluorescence intensities are indicated in arbitrary units (a.u.). Signal intensity profiles are provided for the cells indicated by asterisks. White arrowheads show the depletion of RplA-mCherry signal at a cell pole.

B Representative microscopy images of DAPI-stained FtsZ-depleted cells (CJW7588) expressing cytoplasmic msfGFP in transition phase in M9gluCAAT supplemented with 0.4% arabinose to induce the CRISPRi system, thereby blocking the expression of *ftsZ*. The corresponding signal intensity profile is shown below. Scale bar: 5 μm.

Fig EV3: Representative image of 2-NBDG incorporation in a filamentous polynucleoid cell in transition phase.

Microscopy images of a cephalexin-treated cell (CJW7324) expressing RplA-mCherry in transition phase (OD 2.0). Yellow arrowheads indicate accumulations of 2-NBDG that sandwich an accumulation of RplA-mCherry signal. Below is the cell signal intensity profile, with the grey shade highlighting the region of interest. Scale bar: 5 μm.

Fig EV4: Normalized constriction offset measurements for the WT and Δ*glgBXCAP* cells from co-culture experiments. Boxplots of the normalized constriction offset in exponential and transition phases for the biological replicates of the co-culture experiments shown in Fig 3C.

Fig EV5: Normalized nucleoid offset measurements for the WT and Δ*glgBXCAP* cells from the co-culture experiments across different growth phases. Boxplots of the normalized nucleoid offset in exponential, transition, early stationary (24 h), and late stationary phase (72 h) for all the biological replicates of the co-culture experiments. Exponential and transition phase data points for Replica 1 of both mixes are shown in Fig 3D.

Fig EV6: Growth rate measurements in the microfluidic device. Plot of the calculated log growth rate as a function of cell generations for the strain CJW7605 (n = 130 lineages). The solid line and shaded region correspond to the average and the 95% confidence interval, respectively.

Fig EV7: FRAP measurements of the fluorescent glycogen sensor dynamics in glycogen-producing cells in transition phase.

A Timelapse images of a glycogen-producing cell in transition phase before and after photobleaching a region of the cell pole with the larger glycogen sensor accumulation. The first image on the left shows the time frame before photobleaching, while the subsequent images represent frames captured after photobleaching at the indicated time. The schematic shows the region that was photobleached. Scale bar: 1 μm.

B Plot showing the evolution of the normalized fluorescence intensity of the glycogen sensor for the unbleached region and the photobleached region of the cell shown in A before and after photobleaching. The inset shows the data before and during photobleaching.

C Histogram of the half-max fluorescence recovery times calculated for 70 cells in which FRAP measurements were obtained.

Fig EV8: Force-distance curve examples of indentation-based AFM experiments.

The experimental conditions and strains are the same as in Fig 7A-C.

A Representative force-distance curves of a cell at regions “On” and “Off” the protein aggregates.

B Same as panel A but for a cell with glycogen condensates.

C Same as panel A but for a glycogen-free cell.

D Representative force-distance curve on the glass substrate is shown as a control.

Fig EV9: Cell height and indentation measurements by AFM microscopy.

The experimental conditions and strains are the same as in Fig 7A-C.

A Plot showing cell height measurements of 21 cells with protein aggregates, 7 cells with glycogen condensates, and 7 cells without glycogen. The cell height information was analyzed from AFM height images collected from more than three biological replicates. Displayed here are the mean values ± the standard deviations. Statistical comparisons were performed using an unpaired two-tailed Student’s t-test.

B Plot showing the indentation depth distributions of 15 cells with protein aggregates, 16 cells with glycogen condensates, and 13 cells without glycogen. Shown are the mean values ± the standard deviations for the total number of indentation events (technical replicates) indicated by the n value. The indentation events were collected from more than three biological replicates.

Fig EV10: Force-distance curve examples of penetration-based experiments

The experimental conditions and strains are the same as in Fig 7D-E. Representative force-distance curves showing membrane puncture events (indicated by the arrow) in the figure inset.

A Representative force-distance curves of a cell at regions “On” and “Off” the protein aggregates.

B Same as panel A but for a cell with glycogen condensates.

C Same as panel A but for a glycogen-free cell.

EXPANDED VIEW VIDEO LEGENDS

Video EV1: Timelapse sequence showing that nucleoids and ribosomes remain closer to the new pole upon division during transition phase.

Montage video showing phase and fluorescence overlays of a representative cell expressing RplA-msGFP and HupA-mCherry (CJW5159) growing and dividing in transition phase. Cells from a culture in late exponential phase (OD = 0.5) were washed in transition phase medium, spotted on an agarose pad containing transition phase medium (OD = 2.63), and imaged every 2 min. Time stamp shows h:min:s.

Video EV2: Timelapse of the MinD-GFP oscillations.

Video of CJW7872 cells in transition phase. *Left*, Overlay between phase contrast and DAPI at time zero. *Right*, Timelapse of the MinD-GFP fluorescence channel (frame rate = 5 seconds). Scale bar: 1 μm. Time stamp shows min:s.

Video EV3: Timelapse sequence showing glycogen condensate fusions in vitro. Timelapse sequence of glycogen droplets labeled with ConA-FITC as they fuse. The sample was made with 10 g/L of glycogen and 20 mM of 3 kDa PEG in IS buffer. Phase contrast (left) and FITC (right) images were acquired every 10 s at 25°C. Time stamp shows h:min:s.

Video EV4: Timelapse sequence of glycogen droplets. Timelapse sequence showing the phase-separated glycogen droplets undergoing fusion events and exhibiting surface wetting. The sample was made with 10 g/L of glycogen and 750 µM of 20kDa PEG in the IS buffer. Phase-contrast images were acquired every 30 s at 25°C. Time stamp shows min:s.

Video EV5: Timelapse sequence of "collapsed" glycogen aggregates. Timelapse sequence showing the "collapsed" phase-separated glycogen undergoing collisions that do not result in fusion events. The sample was made with 10 g/L of glycogen and 30 mM of 3kDa PEG in the IS buffer. Phase-contrast images were acquired every 10 s at 25°C. Time stamp shows h:min:s.

Video EV6: Z-stack sequence of glycogen condensates excluding GFP. Z-stacks of both phase contrast and GFP of glycogen droplets floating in the sample. Each frame corresponds to a step of 0.125 µm, starting from a point 1.75 µm above the glass surface (z = 0 nm). The sample was prepared with glycogen (10 g/L) in IS buffer mixed with GFP (15 µM) and 100 kDa PEG (200 µM). The imaging was performed at 30°C.

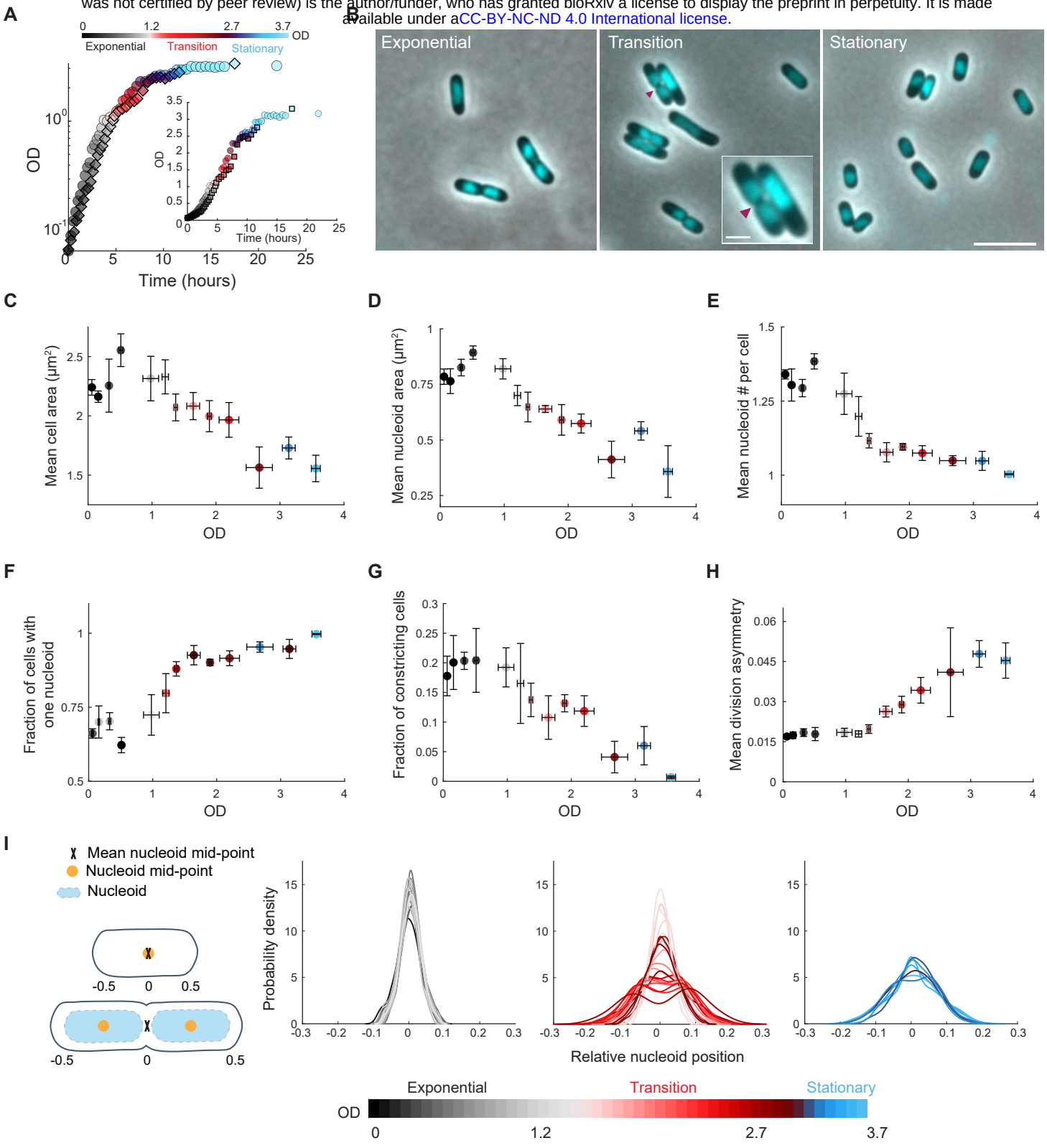

Fig 1

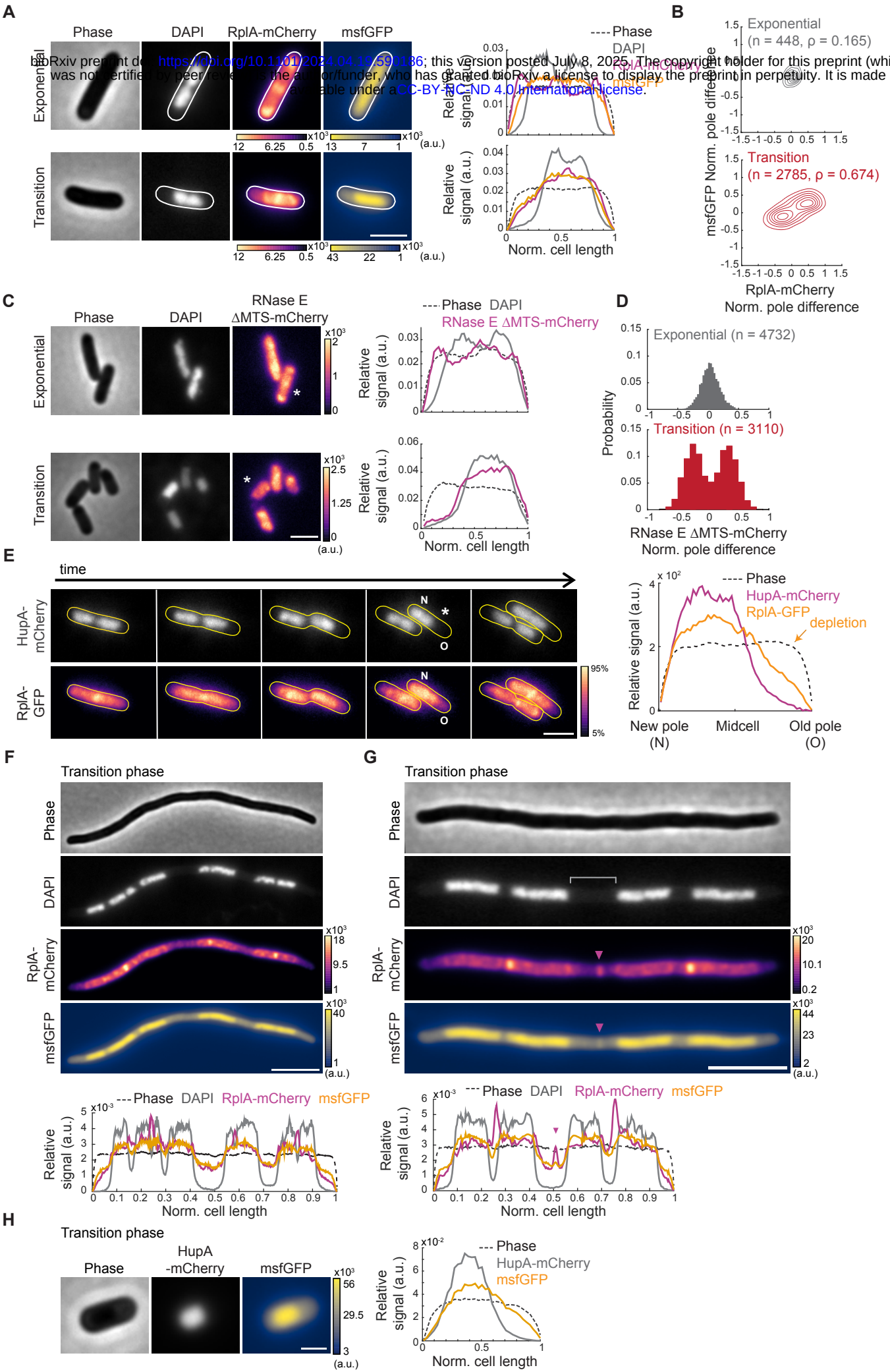

Fig 2

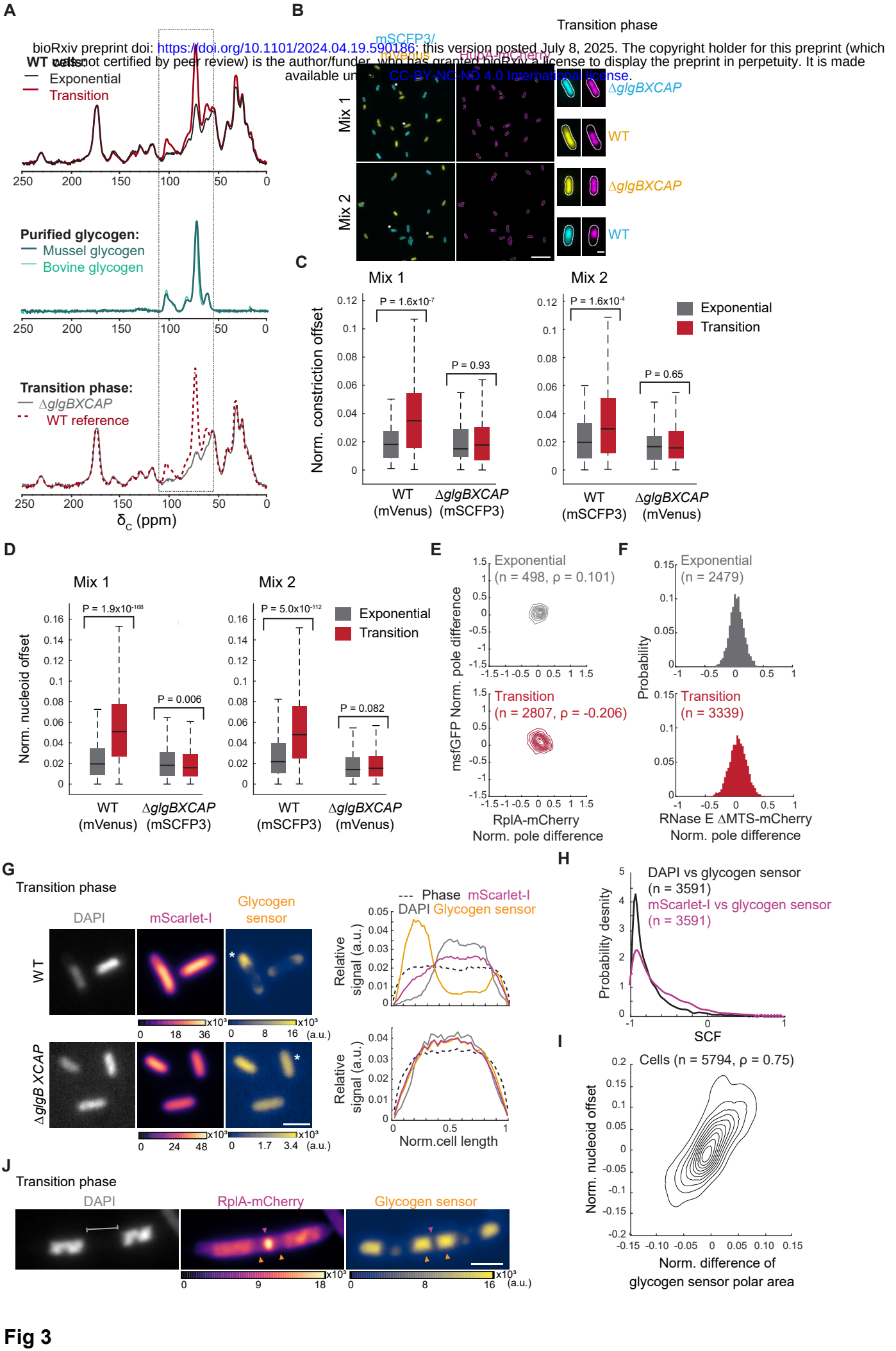

Fig 3

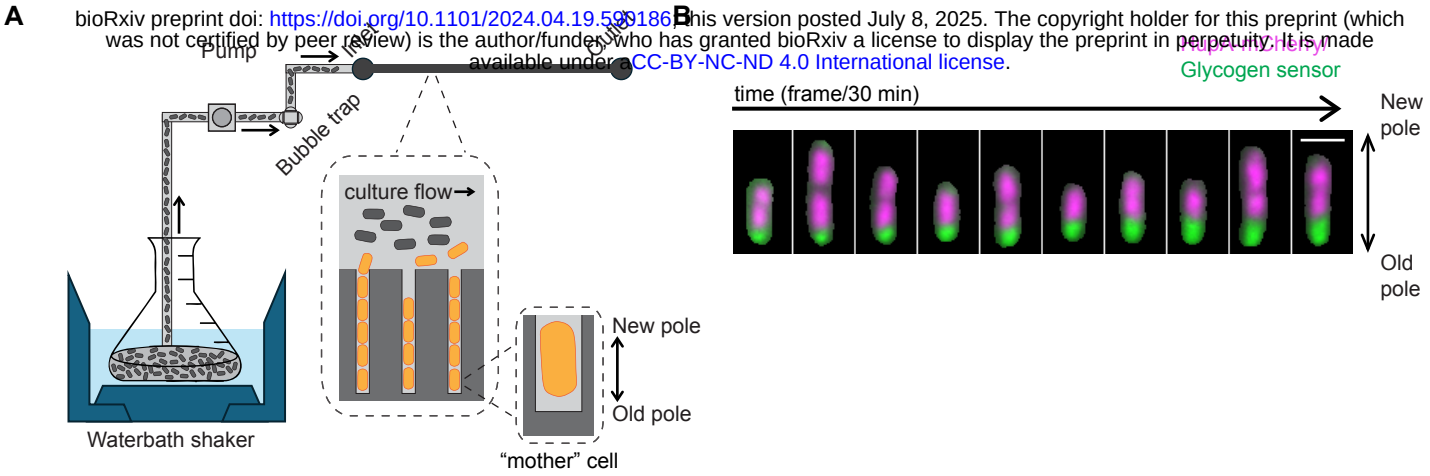

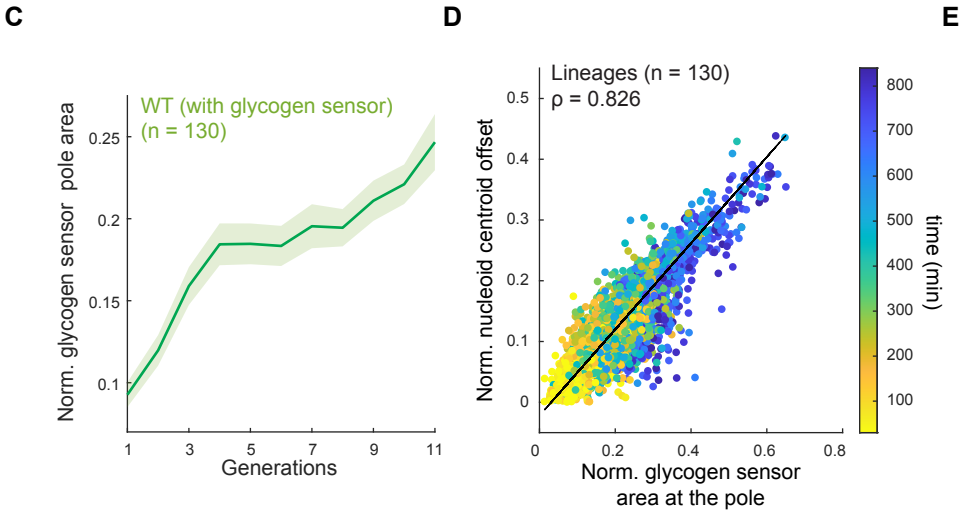

Fig 4

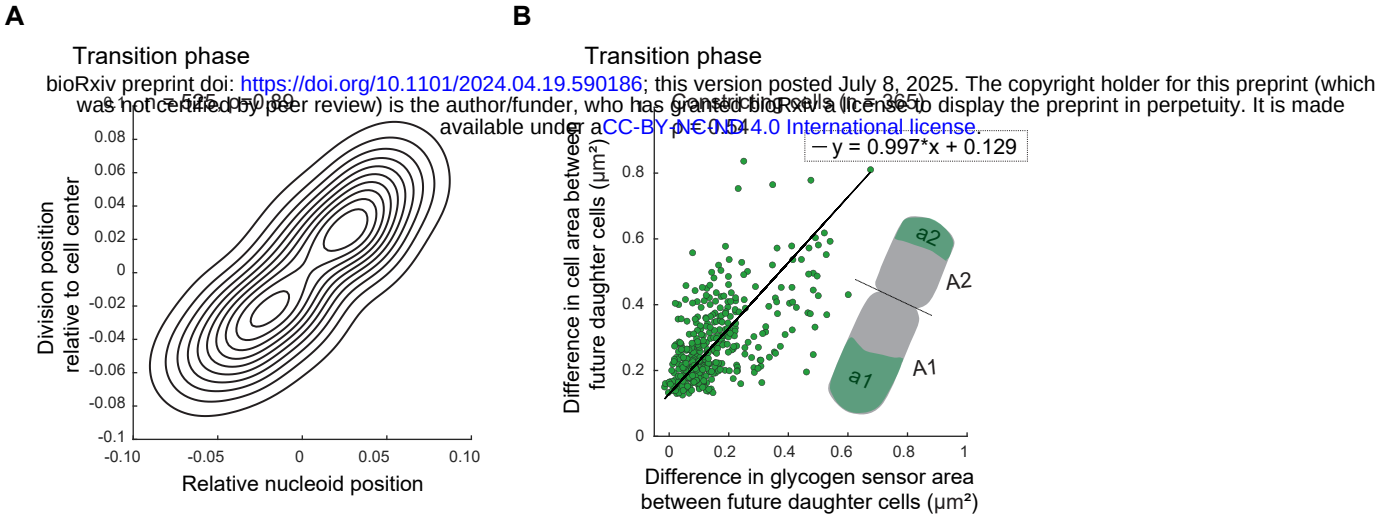

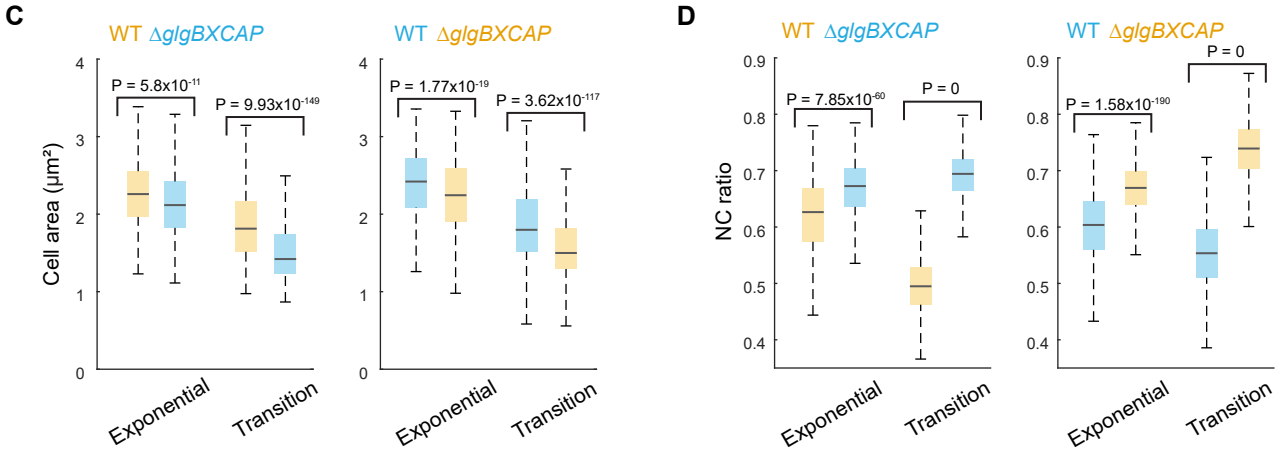

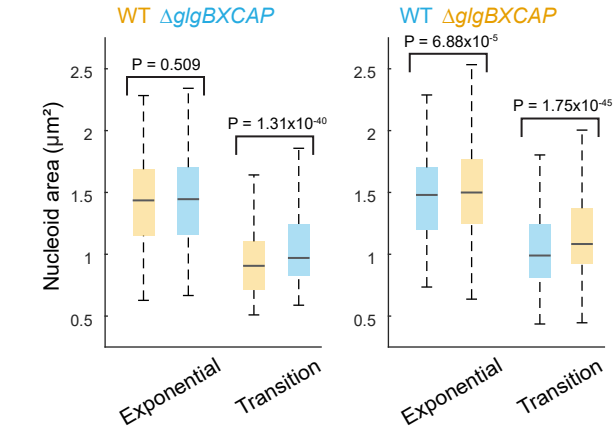

Fig 5

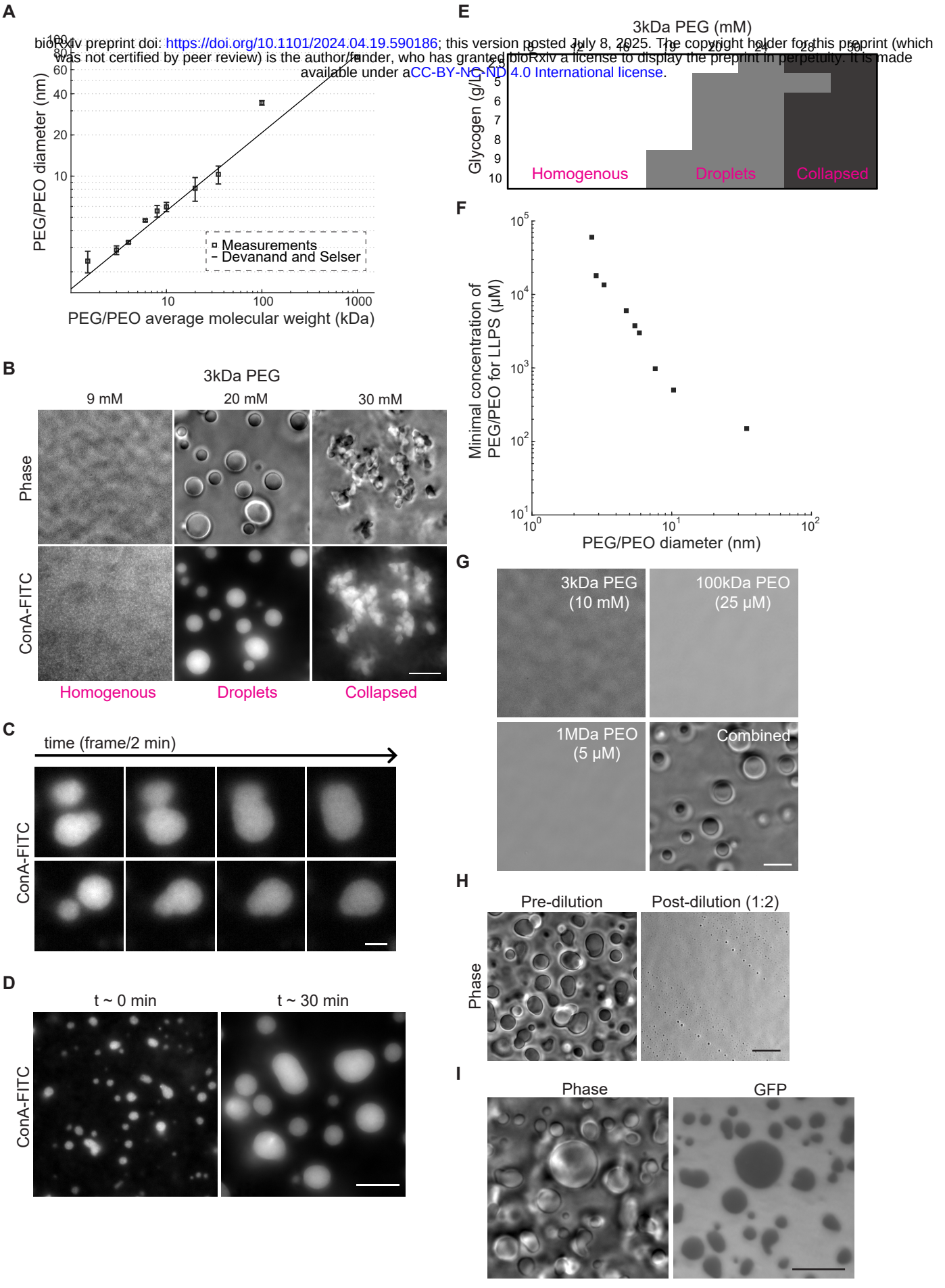

Fig 6

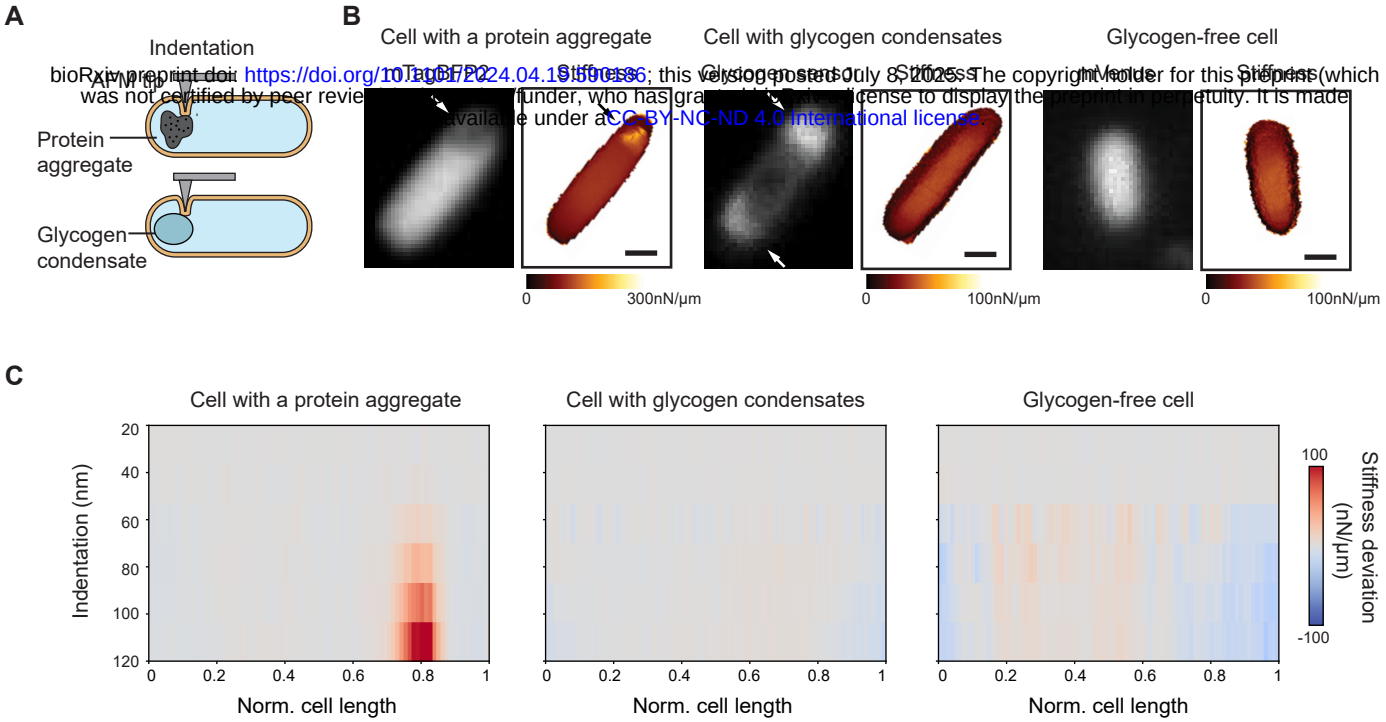

Fig 7